intron/exon boundary mutations are found in 20–30%. *PLP1* deletion is extremely rare. Functional studies have revealed that PMD's wide clinical spectrum is associated with distinct molecular pathogeneses of different mutations in the *PLP1* gene [1]. Meanwhile, phenotypic consequence and the molecular basis of intronic mutations are often difficult to predict [2,3]. Most intronic mutations are expected to alter splicing and result in aberrant transcripts. Here, we report one patient with a mild form of PMD who carries a mutation near the acceptor site of intron 3.

2. Materials and methods

2.1. Patient

A 7-year-old boy was born uneventfully at full term to unrelated Japanese parents. No family history was noted including his mother and an elder brother. He gained head control at 3 months, could sit without support at 10 months, and could walk with assistance at 16 months. He could speak a few words at 2 years of age. When he saw a pediatric neurologist because of his developmental delay, no stridor or nystagmus was noted, but his muscle tone was hypotonic with all extremities displaying exaggerated tendon reflexes and bilateral extensor plantar responses. No cerebellar signs or involuntary movements were observed. No biochemical abnormalities were noted in a routine laboratory examination. Nerve conduction velocities and electromyographic studies were all normal. Auditory brain response elicited only wave I. Brain MRI revealed the completion of myelination and a subependymal cyst in the right frontal region in the T1 signal. Myelination was incomplete in the insula and optic radiation in the T2 signal (Fig. 1).

2.2. DNA sequencing and reverse transcription-polymerase chain reaction analysis

Genomic DNA from the patient was prepared from peripheral blood. Polymerase chain reaction (PCR) amplification of seven exons and promoter regions of the *PLP1* gene was performed, followed by direct sequencing, as previously described [4]. Total RNA isolated from leukocytes was utilized for reverse transcription (RT) reactions to synthesize cDNA, which was then amplified by nested RT-PCR using a primer set spanning exons 3 and 5. Amplified PCR products were subcloned and sequenced.

2.3. In silico splice site prediction

To evaluate potential changes in the splicing efficiency, we performed computational prediction of the splice site selection using online programs: Berkeley Drosophila Genome Project, Splice Site Prediction by Neural Network [5], Human Splicing Finder including Maximum Entropy Modeling [6,7], and Alternative Splice Site Predictor [8]. The 1377-bp wild-type and mutant sequences including intron 3 and adjacent upstream and downstream exons were simultaneously analyzed.

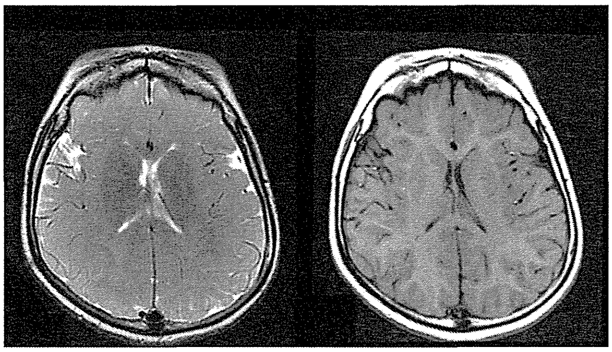

Fig. 1. Brain MRI of the patient at 5 years. Left panel; T2-weighted image shows symmetrical high intensity areas involving the insula and optic radiation, suggesting incomplete myelination. Right panel; T1-weighted image shows high intensity at whole white matter and completion of myelination.

3. Results

Direct sequencing of the patient's *PLP1* exons, exon/intron boundaries, and a promoter region revealed the novel non-coding mutation NM_000533.4:c.454-9T>G in intron 3, located 9 bp upstream of the intron 3/exon 4 boundary (Fig. 2A). No other sequence alterations were found and this mutation was not detected in more than 200 alleles from control Japanese DNA or public databases (dbSNP, 1000 Genomes, Exome Sequencing Project 6500, and Human Genetic Variation Database). The patient's mother was heterozygous for this mutation. Sequencing of the cloned RT-PCR products from the patient's cDNA revealed aberrant and normal transcripts (Fig. 2B and C). The aberrant transcripts revealed a cryptic DM20 mRNA (alternative splicing variant) in which the 5′ donor site of exon 3 is joined to intron 3 at 118 bp upstream of the normal 3′ acceptor site (r.348_349ins349-118_349-1;DM20int3δ) (Fig. 2D). This aberrant splicing is predicted to add 7 residues to the exon 3-coded amino acid sequence followed by a stop codon, leading to premature termination of translation (p.Phe117GlufsX7;DM20). Only *DM20* transcripts were found both in the patient and control; no *PLP1* transcripts were detected.

In silico prediction analyses using multiple programs commonly showed some effects of this mutation on splicing (Table 1). Likelihood scores for the native 3′ acceptor site were reduced by the mutation in 3 of 4 programs. This reduction probably results from an

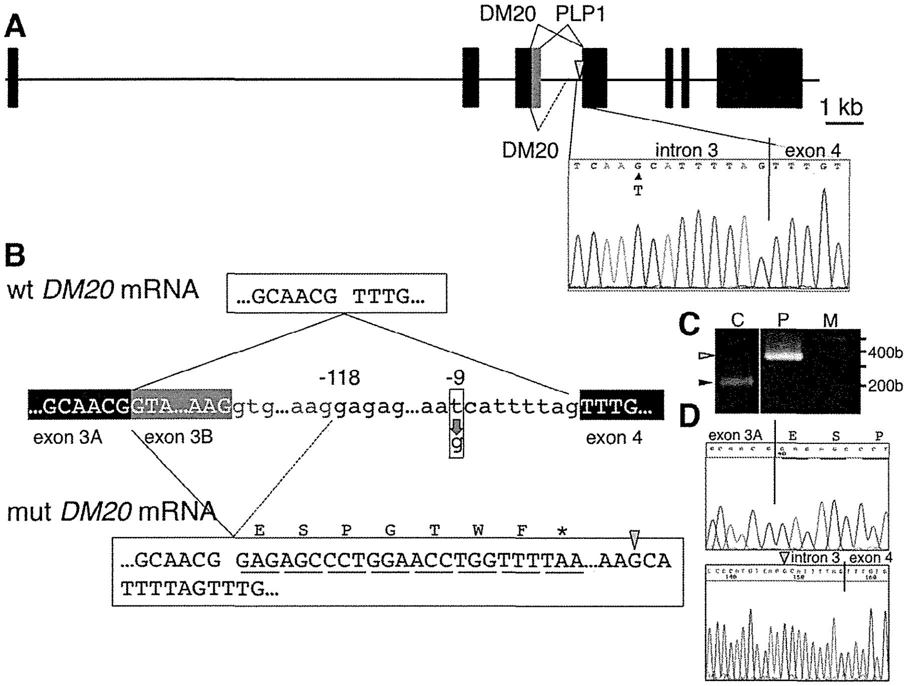

Fig. 2. *PLP1* mutation found in intron 3. (A) Genomic structure of the *PLP1* gene showing exon1 to 7 (boxes) with a normal alternative splicing pattern of PLP1/DM20 above the horizontal line and an aberrant splicing pattern detected in this study below. PLP1-specific part of exon 3 (exon 3B) is shown as gray box. The arrowhead indicates the c.545–9T>G mutation. Sequence chromatogram at the splicing junction is shown. (B) Nucleotide sequences from exon 3A (common to DM20 and PLP1) to exon 4. The T>G substitution at −9 nt is shown in a rectangle. Above shows wild-type DM20 mRNA with lines indicating splicing from exon 3A to exon 4; below shows the mutant DM20 mRNA with aberrant splicing from exon 3A to −118 nt. Underlined nucleotides indicate putatively translated codons after exon 3A (and possibly exon 3B, although this was undetectable by our analysis using leukocytes) followed by a premature stop codon (asterisk). (C) Agarose gel electrophoreses of RT-PCR fragments obtained from a control (C) and the patient (P). Size marker (M). Two nested-PCR primer sets are designed between exon3A and exon5 for the first round (TCCAGTATGTCATCTATGGAACTGCC/CCACAAACCTTGCCAGGGAAA), and exon3A and exon4/5 (CACCATACATTCTGGCATCAGC/GCGCAGTCAGGCAGATCTTT) for the second round, which normally produces a 237 bp band of *DM20* (black arrowhead). However, the patient's sample results in a 355 bp abnormal band (gray arrowhead) in addition to a faint 237 bp normal band. (D) Sequence chromatogram showing the start point (top) and the intron3/exon4 junction (bottom) of the aberrant splicing product obtained from the patient's 355 bp RT-PCR fragments in C. The Letters show deduced amino acid residues that are also seen in B.

Table 1
Splicing sites predictions.

	Native splicing site (WT/Mut)	Aberrant transcript
BDGP	0.46/0.10↓	nd
HSP (Matrices)	75.77/72.68	84.36
HSP (MaxEnt)	6.75/−0.07↓	6.13
ASSP	3.082/1.169↓	5.071

Scores predicted by each program are shown. The effect of c.454-9T>G was predicted by comparing wild-type (WT) and mutant (Mut) sequences. BDGP, Berkeley Drosophila Genome Project, Splice Site Prediction by Neural Network; HSP, Human Splicing Finder; MaxEnt, Maximum Entropy; ASSP, Alternative Splice Site Predictor; nd, not detected. Arrows indicate the score for mutation considerably lower than wild-type.

interruption of the poly-pyrimidine tract, which is usually present upstream of acceptor site and interact with poly-pyrimidine tract binding proteins to regulate splicing. The acceptor site detected by the RT-PCR analysis showed a higher likelihood score than the native acceptor site in 3 programs.

4. Discussion

Here we report one patient with an unusually mild form of PMD caused by the novel intronic mutation c.454-9T>G that disrupts *PLP1* splicing. This patient presented at the mildest end of the clinical severity spectrum, which overlaps with spastic paraplegia type 2, showing later onset and relatively good motor development, and achieving independent walking or walking with assistance [9]. Intellectual disability was also mild. This mild phenotype has been observed in patients with *PLP1* deletions, truncating mutations, and PLP1-specific exon 3B mutations, or rarely in those with amino acid substitutions at specific residues as well as some with intronic mutations, but is unusual in most PMD patients caused by amino acid substitutions or duplications.

Sequencing of the patient's cDNA and *in silico* prediction analysis results suggest that the intronic alteration likely diminishes exon 4 acceptor activity, leading to the use of a cryptic site. The resultant transcript inserted the last 118 bp of intron 3 after exon 3, putatively leading to a premature truncation codon shortly thereafter. This aberrant mRNA may be subject to nonsense-mediated decay and rapid disruption before translation. Therefore, we expect that this intronic mutation may result in a reduced expression of normal protein, presumably leading to a mild phenotype.

Of the 37 splicing mutations reported in the literature, 17 are located in intron 3 [10]. One mutation, c.454-10A>G, located 1 bp upstream of the present mutation, was found in a patient with mild PMD [2]. Expression analysis using patient-derived fibroblasts demonstrated at least 3 aberrant transcripts. All of these transcripts putatively result in premature termination; therefore, the c.454-10A>G mutation causes a null allele regardless of which cryptic site is dominantly utilized. Although the actual sites for cryptic splicing may be different from our patient, it is probably common that altered transcripts all result in null alleles and lead to a mild clinical phenotype in both cases.

The major limitation of our expression study was the use of blood leukocytes, which express only a trace of *PLP1/DM20* transcript. Skin fibroblasts may serve as a better resource for *PLP1* expression study, potentially enabling more sensitive detection of aberrant transcripts. Unfortunately, we were unable to obtain such patient's materials to exclude the possibility for other variant transcripts.

Acknowledgements

We thank the patient and his family for their participation to this study. This study was supported in part by grants from the Japan Agency for Medical Research and Development, AMED (Practical Research Project for Rare/Intractable Diseases,15ek0109016 to K.I., K. K., and H.O.), Health Labour Sciences Research Grant (H27-Nanchitou-ippan-020, K.I., K.K., and H.O.), and Grant-in-Aid for Scientific Research (Kiban(B): 15H04878 to K.I. and H.O.).

References

[1] Inoue K. PLP1-related inherited dysmyelinating disorders: Pelizaeus-Merzbacher disease and spastic paraplegia type 2. Neurogenetics 2005;6:1–16.

[2] Bonnet-Dupeyron MN, Combes P, Santander P, Cailloux F, Boespflug-Tanguy O, Vaurs-Barriere C. PLP1 splicing abnormalities identified in Pelizaeus-Merzbacher disease and SPG2 fibroblasts are associated with different types of mutations. Hum Mutat 2008;29:1028–36.

[3] Hobson GM, Davis AP, Stowell NC, Kolodny EH, Sistermans EA, de Coo IF, et al. Mutations in noncoding regions of the proteolipid protein gene in Pelizaeus-Merzbacher disease. Neurology 2000;55:1089–96.

[4] Osaka H, Kawanishi C, Inoue K, Onishi H, Kobayashi T, Sugiyama N, et al. Pelizaeus-Merzbacher disease: three novel mutations and implication for locus heterogeneity. Ann Neurol 1999;45:59–64.

[5] Reese MG, Eeckman FH, Kulp D, Haussler D. Improved splice site detection in Genie. J Comput Biol 1997;4:311–23.

[6] Desmet FO, Hamroun D, Lalande M, Collod-Beroud G, Claustres M, Beroud C. Human Splicing Finder: an online bioinformatics tool to predict splicing signals. Nucleic Acids Res 2009;37:e67.

[7] Yeo G, Burge CB. Maximum entropy modeling of short sequence motifs with applications to RNA splicing signals. J Comput Biol 2004;11:377–94.

[8] Wang M, Marin A. Characterization and prediction of alternative splice sites. Gene 2006;366:219–27.

[9] Cailloux F, Gauthier-Barichard F, Mimault C, Isabelle V, Courtois V, Giraud G, et al. Genotype-phenotype correlation in inherited brain myelination defects due to proteolipid protein gene mutations. Eur J Hum Genet 2000;8:837–45.

[10] Stenson PD, Mort M, Ball EV, Shaw K, Phillips A, Cooper DN. The human gene mutation database: building a comprehensive mutation repository for clinical and molecular genetics, diagnostic testing and personalized genomic medicine. Hum Genet 2014;133:1–9.

Neurobiology of Disease 80 (2015) 1–14

Contents lists available at ScienceDirect

Neurobiology of Disease

journal homepage: www.elsevier.com/locate/ynbdi

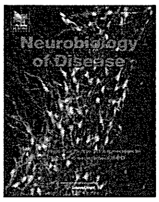

Additive dominant effect of a *SOX10* mutation underlies a complex phenotype of PCWH

Yukiko Ito [a,b,1], Naoko Inoue [a,1], Yukiko U. Inoue [c,1], Shoko Nakamura [a], Yoshiki Matsuda [d], Masumi Inagaki [d], Takahiro Ohkubo [a], Junko Asami [c], Youhei W. Terakawa [c,e], Shinichi Kohsaka [f], Yu-ichi Goto [a], Chihiro Akazawa [f,g], Takayoshi Inoue [c], Ken Inoue [a,*]

[a] *Department of Mental Retardation and Birth Defect Research, National Institute of Neuroscience, National Center of Neurology and Psychiatry (NCNP), Ogawahigashi, 4-1-1, Kodaira, Tokyo 187-8502, Japan*
[b] *Department of Molecular Neuroscience, Medical Research Institute, Tokyo Medical and Dental University (TMDU), 1-5-45 Yushima, Bunkyo-ku, Tokyo 113-8510, Japan*
[c] *Department of Biochemistry and Cellular Biology, National Institute of Neuroscience, NCNP, 4-1-1 Ogawahigashi, Kodaira, Tokyo 187-8502, Japan*
[d] *Department of Developmental Disorders, National Institute of Mental Health, NCNP, 4-1-1 Ogawahigashi, Kodaira, Tokyo 187-8502, Japan*
[e] *Division of Morphological Neuroscience, Gifu University Graduate School of Medicine, 1-1 Yanagito, Gifu, Gifu 501-1194, Japan*
[f] *Department of Neurochemistry, National Institute of Neuroscience, NCNP, 4-1-1 Ogawahigashi, Kodaira, Tokyo 187-8502, Japan*
[g] *Department of Biochemistry and Biophysics, Graduate School of Health Care Sciences, TMDU, 1-5-45 Yushima, Bunkyo-ku, 113-8510 Tokyo, Japan*

ARTICLE INFO

Article history:
Received 2 August 2014
Revised 26 April 2015
Accepted 29 April 2015
Available online 7 May 2015

Keywords:
PCWH
Mutant *SOX10*
BAC transgenic mouse

ABSTRACT

Distinct classes of *SOX10* mutations result in peripheral demyelinating neuropathy, central dysmyelinating leukodystrophy, Waardenburg syndrome, and Hirschsprung disease, collectively known as PCWH. Meanwhile, *SOX10* haploinsufficiency caused by allelic loss-of-function mutations leads to a milder non-neurological disorder, Waardenburg–Hirschsprung disease. The cellular pathogenesis of more complex PCWH phenotypes in vivo has not been thoroughly understood. To determine the pathogenesis of PCWH, we have established a transgenic mouse model. A known PCWH-causing *SOX10* mutation, c.1400del12, was introduced into mouse Sox10-expressing cells by means of bacterial artificial chromosome (BAC) transgenesis. By crossing the multiple transgenic lines, we examined the effects produced by various copy numbers of the mutant transgene. Within the nervous systems, transgenic mice revealed a delay in the incorporation of Schwann cells in the sciatic nerve and the terminal differentiation of oligodendrocytes in the spinal cord. Transgenic mice also showed defects in melanocytes presenting as neurosensory deafness and abnormal skin pigmentation, and a loss of the enteric nervous system. Phenotypes in each lineage were more severe in mice carrying higher copy numbers, suggesting a gene dosage effect for mutant *SOX10*. By uncoupling the effects of gain-of-function and haploinsufficiency in vivo, we have demonstrated that the effect of a PCWH-causing *SOX10* mutation is solely pathogenic in each SOX10-expressing cellular lineage in a dosage-dependent manner. In both the peripheral and central nervous systems, the primary consequence of *SOX10* mutations is hypomyelination. The complex neurological phenotypes in PCWH patients likely result from a combination of haploinsufficiency and additive dominant effect.

Introduction

Peripheral demyelinating neuropathy, central dysmyelinating leukodystrophy, Waardenburg syndrome, and Hirschsprung disease (PCWH, OMIM #609136) is a rare inherited disorder caused by distinct classes of *SOX10* (Sry-like box 10) mutations (Inoue et al., 1999, 2002, 2004; Pingault et al., 2000; Touraine et al., 2000). SOX10 belongs to the SOX transcription factor family, which commonly contains a high-mobility group (HMG) DNA-binding domain and plays important roles in the determination of cell fate with specific functions in development (Chew and Gallo, 2009; Gubbay et al., 1990; Kamachi and Kondoh, 2013). *SOX10* regulates the development and maintenance of neural crest derivatives including Schwann cells, melanocytes, and enteric ganglion cells, and of oligodendrocytes, which are not derived from the neural crest (Bondurand and Sham, 2013; Kuhlbrodt et al., 1998; Mollaaghababa and Pavan, 2003). Accordingly, *SOX10* gene mutations result in a wide spectrum of clinical phenotypes involving these cells. While PCWH involves all four cell lineages, *SOX10* mutations can also

---

[*] Corresponding author. Fax: +81 42 346 1743.
E-mail addresses: c57bl6j@excite.co.jp (Y. Ito), inouenok@yahoo.co.jp (N. Inoue), yinn3@ncnp.go.jp (Y.U. Inoue), ramukana@ncnp.go.jp (S. Nakamura), yoshiki_0430@yahoo.co.jp (Y. Matsuda), inagaki@ncnp.go.jp (M. Inagaki), galoistaka@gmail.com (T. Ohkubo), asami@ncnp.go.jp (J. Asami), y_tera@gifu-u.ac.jp (Y.W. Terakawa), kohsaka@ncnp.go.jp (S. Kohsaka), goto@ncnp.go.jp (Y. Goto), c.akazawa.bb@tmd.ac.jp (C. Akazawa), tinoue@ncnp.go.jp (T. Inoue), kinoue@ncnp.go.jp (K. Inoue).

[1] These authors contributed equally to this work.**Available online on ScienceDirect (www.sciencedirect.com).**

http://dx.doi.org/10.1016/j.nbd.2015.04.013

cause Waardenburg–Hirschsprung disease (WS4; OMIM #277580), which is characterized by sensory deafness with hypopigmentation and aganglionic megacolon, resulting from developmental failure of melanocytes and enteric ganglion cells, respectively (Bondurand et al., 2007; Pingault et al., 1998, 2002). In addition, *SOX10* mutations also cause Kallmann syndrome (OMIM #611584) with deafness (Pingault et al., 2013). Mutations in *SOX10* may result in an extremely wide range of clinical manifestations.

The mechanisms by which different mutations in the *SOX10* gene cause different clinical phenotypes have only been partially determined. It is poorly understood why different *SOX10* mutations result in the neurological phenotypes in PCWH, ranging from mild neuropathy and subtle hypomyelination in the brain to severe congenital hypomyelinating neuropathy and leukodystrophy. Most patients with *SOX10*-associated diseases are sporadic cases, often with de novo heterozygous mutations that presumably act as dominant alleles. In vitro and in vivo analyses indicate that mutations are likely to act as loss-of-function alleles in WS4, and SOX10 haploinsufficiency is the expected mechanism for WS4 (Inoue et al., 1999, 2002, 2004; Pingault et al., 2000; Touraine et al., 2000). In contrast, in vitro findings suggest that PCWH-causing mutations function as either dominant-negative or gain-of-function alleles (Inoue et al., 2004; Pingault et al., 1998). Most *SOX10* mutations result in premature termination codons; those in the upstream exons cause WS4, whereas those in the last exon lead to PCWH. This difference depends on whether they trigger or escape nonsense-mediated mRNA decay (Inoue et al., 2004). A few PCWH cases have unique mutations that disrupt the putative stop codon and extend translation into the 3′ untranslated region (UTR) (Inoue et al., 1999; Sham et al., 2001). In vitro functional analysis has demonstrated that the SOX10 extension mutant completely loses its DNA binding ability and transcriptional activity, and part of extended region gains a deleterious function (Inoue et al., 2007). Nevertheless, there is no in vivo evidence to date that adequately explains the complex phenotypes of PCWH.

Several lines of mouse models have been established to determine the pathogenesis of the *SOX10*-associated diseases. *Dominant megacolon* (*Sox10*$^{dom/+}$), a spontaneous mutant, (Herbarth et al., 1998; Southard-Smith et al., 1998, 1999) and a heterozygous *Sox10* knockout (*Sox10*$^{lacZ/+}$) mouse (Britsch et al., 2001) serve as models for WS4. *Sox10*^{dom}*/dom* and *Sox10*$^{lacZ/lacZ}$ mice are both embryonically lethal and exhibit severe deficits in the organogenesis of neural crest lineages (Britsch et al., 2001; Southard-Smith et al., 1998). However, no mouse model has yet been available to mimic the pathology of PCWH.

In this study, we have used recombinant bacterial artificial chromosome (BAC) transgenic techniques to establish a mouse model carrying a PCWH-causing mutation (Inoue et al., 1997, 2008) and delineated the mechanism underlying the complex neurological phenotypes of human PCWH patients.

Materials and methods

Generation of BAC transgenic mouse lines

All animal experiments in this study conform to Japanese governmental guidelines and have been approved by the Animal Care and Use Committee of the National Institute of Neuroscience, Japan (Projects #2007022 and #2011007). In order to generate the *SOX10* c.1400del12 mutation (termed S1; Inoue et al., 2007)-bearing transgenic mouse lines, a mouse BAC clone *RP24-85O14* (CHIORI, BACPAC Resources) containing the entire *Sox10* gene was modified by means of recombineering (Copeland et al., 2001; Lee et al., 2001). The design of this recombineering, including arm configuration for homologous recombination and bacterial selection by neomycin (Neo) gene expression, has been described previously (Inoue et al., 1997; a flowchart summary in Fig. 1A). Modified BAC clones were enzymatically linearized at a PI-*SceI* site (Fig. 1A), dialyzed and diluted to ~2 ng/μL for pronuclear injection into fertilized eggs collected from a superovulated B6C3F1 (a hybrid of C57BL/6 and C3H/He) mouse strain (SLC, Japan), as detailed previously (Shibata et al., 2010). Generation of the *Sox10::Venus* BAC transgenic mouse lines was described previously (Shibata et al., 2010), and those with 2-copy and 20-copy transgene integrations were analyzed.

Evaluation of transgene integration and copy number in founders and their maintenance

Tail DNA was collected from founder mice for genotyping. The PCR primer sets used for determining transgene integration are listed (Table 1), and the target sequence is indicated by a bar 1 in the schematic (Fig. 1A). For the transgene positive founders, the presence of the *RP24*-BAC vector end sequences (indicated by dots 3 and 4 in Fig. 1A) was always confirmed by PCR to minimize the possibility that fortuitous deletions occurred on the BAC construct that was integrated into the mouse chromosome, as described previously (Shibata et al., 2010). For evaluations of the transgene copy number, TaqMan probes for quantitative PCR (Table 1) were designed to target region 2, indicated by a bar (Fig. 1A).

Both the *SOX10-S1* transgenic (Tg) mouse lines 55 and 196 (L55 and L196) were maintained on a B6C3 background. L55 is biallelic (Fig. 1B), and double hemizygous mice with three copies of the transgenes (3Tg mice) were maintained by mating with Jcl:B6C3F1 wild-type (Wt) mice (CLEA Japan Inc.). Single hemizygous mice with two tandem copies of the transgene (2Tg mice; Fig. 1B) and 3Tg mice were intercrossed to generate various genotypes of mice with Wt or 1 to 5 copies of *SOX10-S1* transgene (1Tg, 2Tg, 3Tg, 4Tg and 5Tg) in L55 (Fig. 1C). To obtain L55-Tg mice as C57Bl/6$_{N3}$, 3Tg mice were backcrossed to C57BL/6JJcl Wt mice (CLEA Japan Inc.) for three generations. For L196, hemizygous mice were mated with Jcl:B6C3F1 Wt mice (CLEA Japan Inc.) for maintenance and analyses.

Evaluation of Venus expression by quantitative RT-PCR

To evaluate the expression levels of the transgene in *SOX10-S1*-Tg mice at P0, total RNA obtained from the spinal cords at cervical to thoracic levels was utilized for Quantitative RT-PCR using a LightCycler® 480 Real-Time PCR system (Roche) for 1Tg ($n = 3$), 2Tg ($n = 5$), 3Tg ($n = 3$), 4Tg ($n = 2$), and 5Tg ($n = 3$) mice in L55, and Tg/− mice in L196 ($n = 4$). We used *Venus* TaqMan-probe and primers that were prepared for the genomic copy number validation with ribonuclease P RNA component H1 (*Rpph1*) as an internal control. All samples were assayed in triplicate. Expression levels of *Venus* were evaluated using the ddCt method according to the manufacturer's protocol. All values of *Venus* were normalized to the mean value for 1Tg mice.

Evaluation of the relative expression levels of human SOX10-S1 transcripts to the endogenous Sox10 transcripts

To evaluate the expression levels of human *SOX10-S1* transgene relative to the endogenous *Sox10* gene, complementary DNA obtained from the P3 spinal cord of 3Tg mice ($n = 3$) in L55 was utilized for RT-PCR. The following primers were used to amplify both human and mouse *SOX10* genes: "ccacgaggtaatgtccaaca" and "gagatccaggcRgagtgtcc". The PCR products were treated with *Pvu*II that can digest only the mouse *SOX10* PCR products, followed by agarose gel electrophoresis to separate the human *SOX10-S1* and endogenous *Sox10*. The gel images were captured using the ChemiDoc™ XRS plus (BioRad) and the intensity of each band was measured using the Image Lab software (BioRad). The values of human *SOX10-S1* product (159 bp) were normalized to those of mouse *Sox10* products (101 bp).

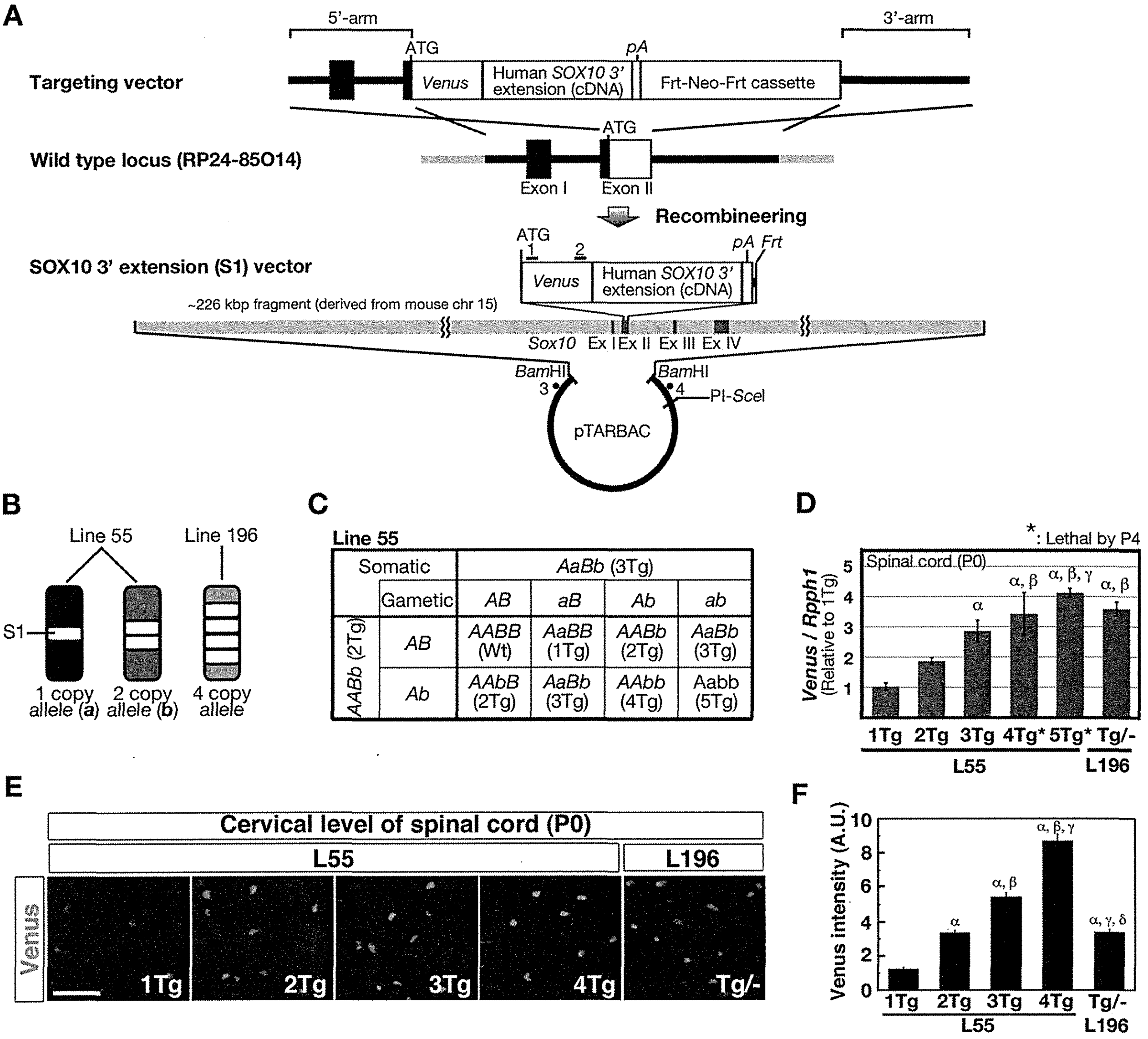

Fig. 1. Generation of mutant *SOX10-Venus* transgenic Lines 55 and 196. (A) A mouse bacterial artificial chromosome (BAC) clone *RP24-85O14* that encompassing 226-kb interval of the *Sox10* gene locus was modified by means of recombineering to express the human *SOX10-Venus* transgene carrying a PCWH-causing 3′ extension mutation (S1). Positions of PCR primers designed for genotyping of mice (regions 1, 3, and 4) are shown. Primers for quantitative PCR target region 2. ATG, translation start site; Ex, exon; Frt, flippase recognition target sequence; Neo, neomycin resistant gene; pA, polyadenylation signal. (B) Schema shows three alleles generated in *SOX10-S1* transgenic mouse lines. Line 55 possesses two unlinked alleles of the *SOX10-S1* transgene: one has single copy of the *SOX10-S1*-vector (represented by allele *a*) and the other contains two tandem copies (represented by allele *b*). Line 196 is monoallelic with four copies of the *SOX10-S1* transgene. (C) The Punnett square for intercrossing within Line 55 to obtain various genotypes. According to the copy number of the transgene, the genotypes are termed wild-type (Wt) or 1–5Tg in Line 55. (D) Relative expression level of the transgene determined by quantitative RT-PCR. Each of the genotype and line name is shown on the x axis. α, β, γ: statistically significant difference compared with 1Tg, 2Tg, and 3Tg, respectively ($p < 0.05$); *: genotypes lethal by postnatal day (P) 4. (E) Arranged are the SOX10-S1-Venus expressing cells at the cervical level of the spinal cord from *SOX10-S1*-Tg L55 and L196 at P0. Scale bar: 50 μm. (F) Intensities of Venus-immunoreactivities (arbitrary unit: A.U.) measured from individual cell ($n = 139$–251) on cryosections of the spinal cord in each genotype are graphed. α, β, γ and δ indicate statistically significant difference compared with 1Tg, 2Tg, 3Tg, and 4Tg, respectively ($p < 0.01$).

Preparation of postnatal tissue samples for histological analyses

Mice at postnatal days (P) 0–20 were anesthetized and sacrificed by transcardial perfusion with 4% paraformaldehyde in phosphate buffered saline (PBS; pH 7.5). Whole intestines, the cervical parts of the spinal cords, and the brain were removed and post-fixed overnight at 4 °C. The intestines were processed for AchE histochemistry. The spinal cords were cryoprotected with 30% sucrose in PBS, embedded, frozen, and sliced into 10-μm-thick coronal cryosections for immunostaining. The brains were sagittally bisected. One hemisphere was cryoprotected with 30% sucrose in PBS, embedded, frozen, and sagittally sliced into 10-μm-thick sections for immunostaining. A piece of the corpus callosum was separated from the other hemisphere, immersed overnight at 4 °C in 2.5% glutaraldehyde and 2% paraformaldehyde in 0.1 M phosphate buffer (PB, pH 7.4), and used for ultrastructural analysis.

Immunostaining of cryosections

Immunostaining was performed according to the standard method. The following primary antibodies were used: GFP (rabbit anti-GFP, MBL, 1:1000), MBP (mouse anti-myelin basic protein, Covance, 1:2000), Olig2 (rabbit anti-Olig2, IBL, 1:500), and Sox10 (goat anti-Sox10, R&D systems, 1:200). Secondary antibodies were donkey anti-rabbit Alexa Fluor® 488, goat anti-mouse Alexa Fluor® 594, goat anti-rabbit IgG-Alexa Fluor® 594, and donkey anti-goat Alexa Fluor® 594 (Invitrogen, 1:200). Sections were mounted using Vectashield mounting media

Table 1
The list of primer and TaqMan probe sequences for genotyping.

Target	Position in Fig. 1A	Primer sequences		TaqMan-probe sequences
PCR				
Venus	1	acgacttcttcaagtccgcc	(Forward)	
		gtgatcgcgcttctcgttgg	(Reverse)	
BAC1	3	acagcagcaaaacgaaaaat	(Forward)	
		ctgaacgttctgatatgttt	(Reverse)	
BAC2	4	gcgcgccaatagtcatgc	(Forward)	
		gccgcaaatttattagagca	(Reverse)	
Real time PCR				
Venus	2	gtccgccctgagcaaaga	(Forward)	cccaacgagaagcg
		tccagcaggaccatgtgatc	(Reverse)	
Rpph1	2	ggtgcctcacctcagccat	(Forward)	tgaactcgcactgctggccgtg
		gccggagcttggaacaga	(Reverse)	

(Vector laboratories) and images were captured using a fluorescent microscope (BX51, Olympus) with a CCD camera (DP70, Olympus).

Evaluation of Sox10-S1-Venus protein expression levels from the P0 spinal cord

The GFP-immunostained sections of the cervical level of the spinal cord in L55 and L196 were used. The mean gray values of individual GFP-positive cells (139 cells for 1Tg, 251 cells for 2Tg, 188 cells for 3Tg, and 211 cells for 4Tg in L55, and 191 for Tg/− in L196) in the sections were measured as an intensity using ImageJ 1.43u software (available from http://imagej.nih.gov/ij/). The GFP-positive cell was defined as a particle with more than value 4 in 8-bit gray scale.

Auditory brainstem responses (ABRs)

Examination of ABRs of Tg or Wt mice was performed as described previously (Inagaki et al., 2006). ABR wave latency for each waveform and the ABR threshold values were collected from 2Tg ($n = 6$), 3Tg ($n = 6$), and Wt ($n = 3$) mice.

Whole-mount AchE histochemistry for evaluation of the hypoganglionosis

The intestines were washed several times with 0.1 M sodium acetate buffer (pH 5.6) and incubated overnight at room temperature (RT) in a solution containing 3 mM cupric sulfate, 16 mM glycine, 4 mM s-acetylcholine iodide (Sigma), tetraisopropyl pyrophosphoramide (Sigma), and 0.1 M sodium acetate (pH 5.6). After several washes with 0.1 M sodium acetate buffer, the signals were developed with 1% sodium sulfide (pH 7.5) at RT for a few minutes to obtain sufficient intensity of signals.

The distal end of the large intestine was evaluated for hypoganglionosis, which was defined as a loss of plexus accompanied by thick fibers. Whole-mount images were captured using a binocular microscope (MZ8, Leica) equipped with a CCD camera (VB-7010, Keyence). Magnified images of intestinal surfaces were captured using a microscope (BX51, Olympus) with a CCD camera (DP70, Olympus). If necessary, intestines were cut to remove intestinal residue and to flatten the surface.

Intercrossing SOX10-S1 transgenic mouse lines with a Cdh6::LacZ-BAC transgenic mouse line and whole-mount detection of β-galactosidase activity and neurofilament immunoreactivity (IR)

Generation of a *Cdh6::LacZ*-BAC transgenic mouse line that recapitulates the characteristic *Cdh6* expression profile along migrating neural crest cells and differentiating Schwann cells (Inoue et al., 1997) was performed as reported previously (Inoue et al., 2008). Male mice from *SOX10-S1* transgenic Lines 55 and 196 were mated with *Cdh6::LacZ*-BAC transgenic females. Embryos were collected at E8.5–E12.5.

Detection of β-galactosidase in the embryos was performed as previously described (Inoue et al., 2008). Coronal 700-μm-thick embryo slices were prepared using a microslicer (DTK-3000, D.S.K. Japan) and processed for neurofilament staining, using a 1:10 dilution of 2H3 supernatant (Hybridoma bank, Iowa University) and 1:250 dilution of horseradish peroxidase-conjugated secondary antibodies for detection, as described previously (Inoue et al., 2008). In order to quantitate the staining profiles, time for fixation, antibody incubation and signal detection was always equalized. Further to justify the quantitation, the embryos were genotyped after finishing the staining. Whole-mount images were captured using a binocular microscope (MZ8, Leica).

Ultrastructural analysis of myelin and Remak bundles, and G-ratio measurement

For the analysis of sciatic nerves, 3 subjects were selected from 6-week old Wt or 3Tg mice. Sciatic nerves fixed with 2.5% glutaraldehyde and 2% paraformaldehyde in 0.1 M PBS (pH 7.4) were processed for ultra-structural analysis using the standard method. Ultrathin sections were observed and photographed using electron microscopy (FETecnai Spirit TEM, FEI). Post-fixed samples of the corpus callosum were also processed to ultrathin sections for electron microscopy.

To evaluate the G-ratio of the sciatic nerves, 1-μm-thick sections were stained with 2% toluidine blue to observe myelin at a magnification of 100× under a light microscope (BX51, Olympus) with a CCD camera (DP70, Olympus). Three images were captured for each sample of sciatic nerve. The inner and outer diameters of myelinated axons in the images were measured using ImageJ 1.43u software to calculate the G-ratio (inner diameter/outer diameter). The correlation between g-ratios and axon diameters, and the comparisons between genotypes, were statistically evaluated using analysis of covariance (ANCOVA).

To analyze the number of axons in Remak bundles, 8500 μm^2 views were randomly selected from electron microscope images of the Wt and L55 3Tg sciatic nerves. Axons were manually counted within each bundle in a selected area.

Quantification of the number of Olig2-expressing cells and the density of MBP-IR

Three sections of spinal cord were used from each individual sample to determine the presence of Olig2-positive cells and MBP-IR. Olig2-positive cells within the regions of interest (ROIs; 0.067 mm^2) set on the dorsal and ventral parts of the spinal cord were manually counted. The Olig2-positive cells were determined using the "Moments" method of auto thresholding by ImageJ 1.43u software. The values from the dorsal and ventral parts were summed and averaged. The density of MBP-IR was also measured using the same software. Circular ROIs were arranged along the ventral edge of spinal cord (prospective white matter) and the mean densities within the ROIs were measured and averaged from three sections for each sample. Data were collected from 3 to 5 mice of each genotype.

Statistical analysis

Statistical analysis was performed using the Tukey–Kramer multiple comparison test following the analysis of variance (ANOVA), unless noted otherwise. All data were reported as means and standard error of the mean (*SEM*).

Results

Generation of mutant SOX10-Venus transgenic mouse Lines 55 and 196

The mutation that we selected for our mouse models was c.1400del12, which was identified in the first PCWH patient reported in the literature (Inoue et al., 1999). The mutation, termed S1, deletes

12 base pairs starting from the second nucleotide of the putative stop codon, eliminating the stop codon and extending translation into the 3′ UTR. This adds 82 amino acids to the Wt SOX10 protein sequence. This mutation is hereafter designated as SOX10 3′extension. Extensive clinical and in vitro functional studies have been performed on this mutation (Inoue et al., 1999, 2007). In order to overexpress the human SOX10 3′ extension mutant protein in vivo, recombineering was used to modify a mouse BAC clone that contains the entire *Sox10* gene (Fig. 1A). With this modified BAC transgenesis, the mutant SOX10-Venus (SOX10-S1) fusion protein could be selectively expressed in endogenous Sox10-expressing cells in mice. Sox10-expressing cells were labeled with Venus protein using the same BAC clone (Shibata et al., 2010). Previous report also confirmed that the fusion of Venus had no influence on the nuclear import and the transcriptional activity of SOX10 in vitro (Rehberg et al., 2002). Incidentally, we considered that it is inappropriate to select the Wt human *SOX10*-mouse *Sox10* BAC transgenic mice as the negative control, since overexpression of SOX10 dominantly affects the neural crest cell fate decisions (Cossais et al., 2010) and/or sex determinations (Seeherunvong et al., 2004; Polanco et al., 2010), producing other complex pathological conditions.

Using PCR to screen 345 newborns delivered from 10 rounds of pronuclear injections, we found that 37 mice harbored the entire length of the BAC construct. From these, two male surviving founders with white hair spots and abnormalities in motor-function were selected and bred to establish the *SOX10-S1*-Tg mouse lines, 55 and 196 (L55 and L196). Two unlinked alleles of the *SOX10-S1* transgene were isolated from L55: one contained a single copy of the *SOX10-S1* transgene, and the other carried two tandem copies of the transgene (Fig. 1B left). On the other hand, L196 was monoallelic, with four copies of the *SOX10-S1* transgene (Fig. 1B right).

Most of the (Tg/−) mice hemizygous for the three alleles isolated from L55 and L196 survived more than 1 year, and had no fertility problems when bred with C57BL/6 and C3H/Ne hybrid mice (B6C3). Furthermore, L55 double Tg/− mice with two alleles, namely 3Tg, were also viable and fertile. Therefore, L55 2Tg and 3Tg mice were intercrossed to obtain 1Tg, 2Tg, 3Tg, 4Tg and 5Tg mice (Fig. 1C). The 4Tg and 5Tg mice with Mendelian inheritance patterns at birth died by postnatal day 4 (P4). Expression levels of the *SOX10-S1* transgene were positively correlated with the copy number by quantitative RT-PCR using the spinal cords from neonatal (P0) *SOX10-S1*-Tg mice. The expression levels in L196 were equivalent to those of 4Tg mice in L55 (Fig. 1D). In addition, we measured the expression levels of the transgene relative to the endogenous Sox10 gene by means of RT-PCR, which was followed by the restriction fragment length polymorphism evaluation of mouse-specific *PvuII* digestion in L55 3Tg mice. As the results, we found that the Tg expression (from 3 copies) was almost half of the endogenous Sox10 expression (from 2 copies; 0.47 ± 0.1, $n = 3$; data not shown). We further quantified the intensity of Venus-immunoreactivities in the spinal cord sections from neonatal *SOX10-S1*-Tg mice, and confirmed that the expression levels of SOX10-S1-Venus fusion protein were well correlated with the transgene copy numbers in L55. The transgenic protein expression of L196 Tg/− mice was equivalent to 2Tg of L55 (Figs. 1E and F).

Collectively, we established two lines of *SOX10-S1*-Tg mice that inherited three alleles of the PCWH-causing *SOX10* mutant gene, stably producing the mutant SOX10 protein under the control of mouse *Sox10* regulatory elements.

SOX10-S1-Tg mice showed typical features associated with Waardenburg–Hirschsprung syndrome

We observed the postnatal phenotypes of the *SOX10-S1*-Tg mice. In L55, hypopigmentation of hair color in the forelock (data not shown) and the trunk (Figs. 2A and B) was present in some 2Tg and 3Tg mice, but never in 1Tg mice. Rotating behavior suggestive of dysequilibrium was seen in some of 2Tg and 3Tg mice. Tests of auditory function of 2Tg and 3Tg mice showed that the wave latencies of ABR were comparable among Wt, 2Tg, and 3Tg mice (Fig. 2C). However, the auditory threshold of 2Tg and 3Tg mice was higher than that of Wt mice (Fig. 2D), demonstrating sensory deafness in 2Tg and 3Tg mice.

In addition to the lethality seen by P4 in 4Tg and 5Tg mice, a small portion of 3Tg mice died around weaning. Inflation of the large intestine in the dead 3–5 Tg mice was seen on autopsy. Whole-mount acetylcholine esterase (AchE) histochemistry was performed to visualize the enteric nerve plexus at P0 and P3. Defects of the nerve plexus, namely hypoganglionosis, were commonly observed in the distal part of the large intestine in 2–5Tg mice (Figs. 2F and H) while the nerve plexus was nearly normal in the proximal part of small intestine (Figs. 2E and G). In the neonatally lethal 5Tg mice, hypoganglionosis expanded over the entire large intestine (Figs. 2I–P). In L196, some of the Tg/− mice also showed hypopigmentation, rotating behavior, and hypoganglionosis. Taken together, we concluded that *SOX10-S1*-Tg mice exhibited typical features associated with Waardenburg–Hirschsprung syndrome.

The prevalence of hypopigmentation, rotating behavior, and hypoganglionosis was assessed in L55 and L196 transgenic mice (Table 2). Although 1Tg mice showed none of these three features, the frequency among 3Tg mice was higher than among 2Tg mice. As the 3Tg mice were double hemizygous for allele "a" from 1Tg and allele "b" from 2Tg (Fig. 1D), we considered that allele "a" from 1Tg mice exerted a pathological effect on these three features. We further found that hypoganglionosis occurred in all of 4Tg and 5Tg mice lethal by P4. In L55, the occurrences of typical features associated with Waardenburg–Hirschsprung syndrome increased in a manner dependent on the copy number of the *SOX10-S1* transgene.

Embryonic Schwann cell incorporation was retarded in a manner related to Sox10-S1 dosage

In order to thoroughly monitor the effects of *SOX10-S1* overexpression at early embryonic stages, *SOX10-S1*-Tg L55 and L196 mice were intercrossed with a reporter transgenic mouse line that recapitulates characteristic *Cdh6* mRNA expression profiles along migrating neural crest cells and differentiating Schwann cells (Inoue et al., 1997, 2008). Mono-allelic L196 mice were examined first, as the segregation pattern was simple after the intercross. Consequently, we found no apparent difference for *Cdh6::LacZ* expression profiles between Wt and *SOX10-S1* expressing embryos at E8.0–E9.5 (Figs. 3A—D), indicating that overexpressed *SOX10-S1* exerts little influence, if any, on the production and/or migration machinery of neural crest cell populations during the earlier developmental stages. This result presents a striking contrast to the experiments on Wt human SOX10 overexpression in the early chicken neural tube, where massive induction of cadherin-7, a marker comparable with mouse Cdh6, took place and increased cadherin-7-positive emigrating neural crest cells (Cossais et al., 2010).

On the other hand, the number of Schwann cells marked by *Cdh6::LacZ* expression was significantly decreased in *SOX10-S1* expressing embryos from L196 at E11.5–E12.5, when neural crest cells start to differentiate at their final destinations (Figs. 3E–L). We therefore examined *Cdh6::LacZ* expression profiles in E11.5–E12.5 embryos from the multi-allelic Tg mouse L55 that produces a variety of genotypes after intercrossing (i.e., L55 0-3Tg). As a result, 3Tg embryos showed more severe phenotypes compared with 2Tg embryos, and that 1Tg embryos had no obvious phenotype for Schwann cell incorporation (Fig. 4). For instance, *Cdh6::LacZ* expressing Schwann cells that were incorporated into the forelimb (fl) or hindlimb (hl) regions at E12.5 showed a gradual decrease in distributive occupancy that coincides with an increase in *SOX10-S1* transgene copy number (arrowheads in Figs. 4E–H). The trend was the same for *Cdh6::LacZ* expressing cells incorporated along the lateral trunk regions at E11.5 (Figs. 4A–D), E12.5 (Figs. 4E–H) and E13.5 (Supplementary Fig. 1). These results obviously demonstrate the dose-related effect of *SOX10-S1* on differentiating Schwann cells at E11.5–E12.5.

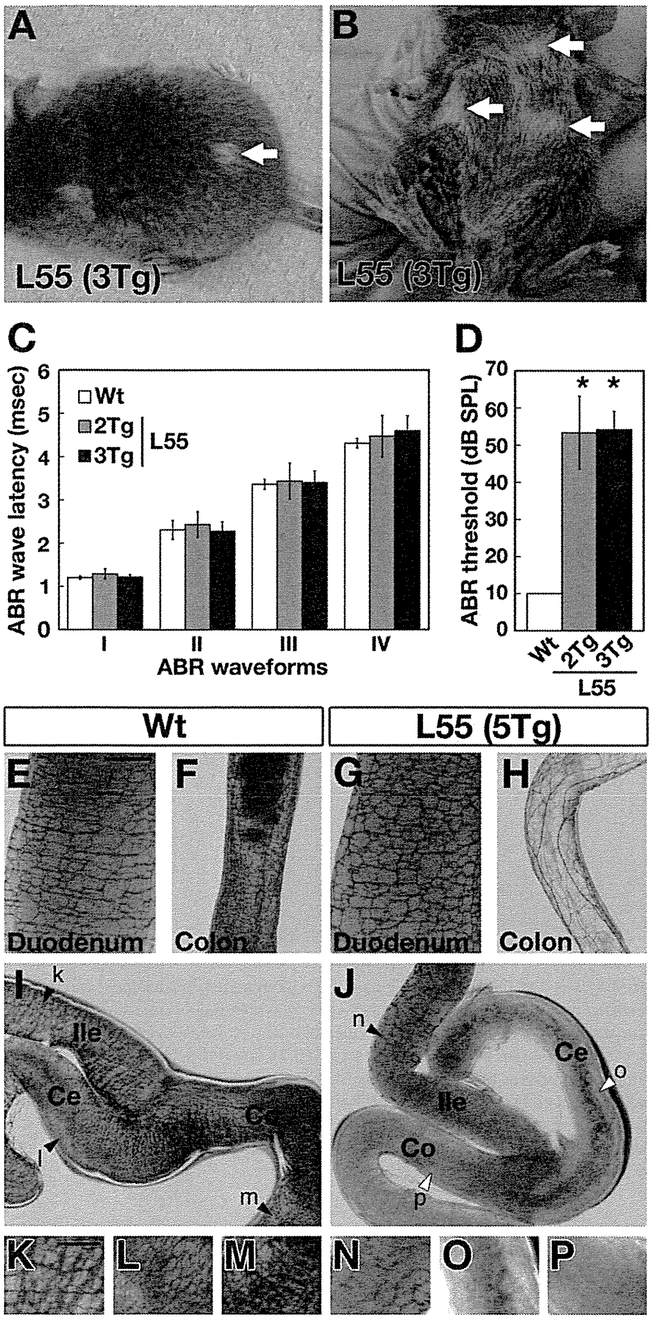

Fig. 2. Waardenburg–Hirschsprung syndrome-associated features in postnatal *SOX10-S1* BAC transgenic mice L55. (A, B) L55 mice showing hypopigmentation of hair color. White spots on the back (white arrow in A) and ventral part of the trunk (white arrows in B) are found in the majority of 3Tg mice. (C, D) The auditory brainstem response (ABR) demonstrated sensory deafness of L55 mice. (C) The latencies of waves I–IV are shown for Wt (white bar), 2Tg (gray bar), and 3Tg (black bar) mice. (D) The auditory threshold of 2Tg and 3Tg mice is higher than that of Wt mice. * represents statistically significant differences from Wt mice ($p < 0.001$). Decibel (dB) is a unit of sound pressure level (SPL). (E–J) Acetylcholine esterase (AchE) histochemistry in Wt (E, F, and I) and 5Tg mice (G, H, and J). The AchE-positive enteric nerve plexus is equivalent to Wt mice at the level of the duodenum (E and G), but is hardly detectable in the distal part of the ileum (Ile), cecum (Ce), and colon (Co) (F, I, H, J). (K–P) These areas indicated by arrowheads in panels I and J are magnified. The lower-case letters of arrowheads corresponds to the uppercase letter of each image. Black arrowheads indicate the area where the AchE-positive enteric nerve plexus is present, and the white ones indicate the absence of the enteric nerve plexus. Scale bars, 500 μm for E to J, and 200 μm for K to P.

Table 2
The occurrence of features associated with Waardenburg–Hirschsprung syndrome in transgenic Lines 55 and 196 during the postnatal period.

Genotype	Hypopigmentation	Dysequilibrium-like rotating behavior	Hypoganglionosis
Line 55			
1 Tg	0% (0/32)	0% (0/32)	0% (0/11)
2 Tg	58% (26/45)	7% (3/45)	4% (1/24)
3 Tg	81% (21/28)	35% (9/26)	14% (2/9)
4 Tg	Unavailable	Unavailable	100% (11/11)
5 Tg	Unavailable	Unavailable	100% (6/6)
Line 196			
Tg/−	54% (7/13)	46% (6/13)	29% (2/7)

The number of the affected/the total number observed is in parentheses. Hypopigmentation and rotating behavior were observed at weaning (4 week old). Rotating behavior did not necessarily coincide with hypopigmentation. Because of death, the total number observed was changed between hypopigmentation and rotating behavior in 3Tg mice of Line 55. Hypoganglionosis was ascertained at P0 and P3.

When E12.5 *Cdh6::LacZ* expressing embryos were co-stained with anti-neurofilament antibodies, *Cdh6::LacZ* expressing cells did not completely associate with the nerves visible as brown signals in L55 3Tg embryos, especially at the caudal trunk regions (Figs. 4J, K, M and N). Noticeably, the degree of motor or peripheral nerve elongation was unchanged, and yet the nerves tended to generate more branches in L55 3Tg embryos (Figs. 4M and N). We assumed that a decrease in the number of *Cdh6::LacZ* expressing Schwann cells could cause expansion of unwrapped areas along the nerves, thereby altering the branching patterns in *SOX10-S1* expressing embryos. Whatever the cause might be, these results clearly indicate that the incorporation of *Cdh6::LacZ* expressing Schwann cells was specifically retarded in L55 3Tg embryos, compared with the normal nerve elongation.

We concluded that expression of the human *SOX10-S1* transgene harboring the PCWH mutation influences Schwann cell differentiation and/or incorporation in a dose-dependent manner, without disturbing initial neural crest cell production and migration at the embryonic stage.

Compact myelin sheaths and Remak bundles were less refined in the sciatic nerve of adult SOX10-S1-Tg mice

Electron microscopy was used to examine the sciatic nerves of 6-week-old L55 3Tg mice to determine whether mutant SOX10-expressing Schwann cells could postnatally affect myelination. In panoramic views of electron micrographs, myelinated axons were similarly arranged in the sciatic nerves of Wt and L55 3Tg mice (Figs. 5A and B). Higher magnification also revealed normally compacted myelin multilayers in L55 3Tg mice (Figs. 5C and D). Moreover, neither demyelinating nor excessive promyelinating profiles, often seen in demyelinating nerves (Anzini et al., 1997; Bremer et al., 2011; Niemann et al., 2000; Perea et al., 2001; Runker et al., 2004; Sereda et al., 1996; Wrabetz et al., 2006), were detected in L55 3Tg mice.

The G-ratio, the ratio of inner to outer diameter of a myelin sheath in a myelinated axon, was measured to determine the thickness of myelin. The G-ratio in 6-week-old L55 3Tg mice was larger than Wt mice, especially in the larger axons, suggesting thinner myelin in L55 3Tg mice (Fig. 5G). This trend was also present in 32-week-old mice (Supplementary Fig. 2), indicating a persistence of the thinner myelin phenotype of the sciatic nerve in L55 3Tg mice. A Similar finding has also been observed in human patients with the PCWH-causing 795delG mutation (Pingault et al., 2000).

In L55 3Tg mice, some Remak bundles (enclosed with a white broken line in Fig. 5F) were enlarged and the space between axons was occasionally narrower (a pair of arrowheads in Fig. 5F), compared with Wt mice. The maximum axon number in a Remak bundle was 50 for L55 3Tg mice and 22 for Wt mice (Fig. 5H). By contrast, there were fewer Remak bundles containing 1–5 axons in L55 3Tg mice compared with Wt mice (Fig. 5H). The median number of axons in a bundle for L55 3Tg mice (6 axons) was statistically larger than that of Wt mice (4 axons; $p = 0.014$, Mann–Whitney *U* test), indicating that the Remak bundles of L55 3Tg mice contain more axons per bundle than those of Wt mice. Collectively, we have demonstrated that compact myelin

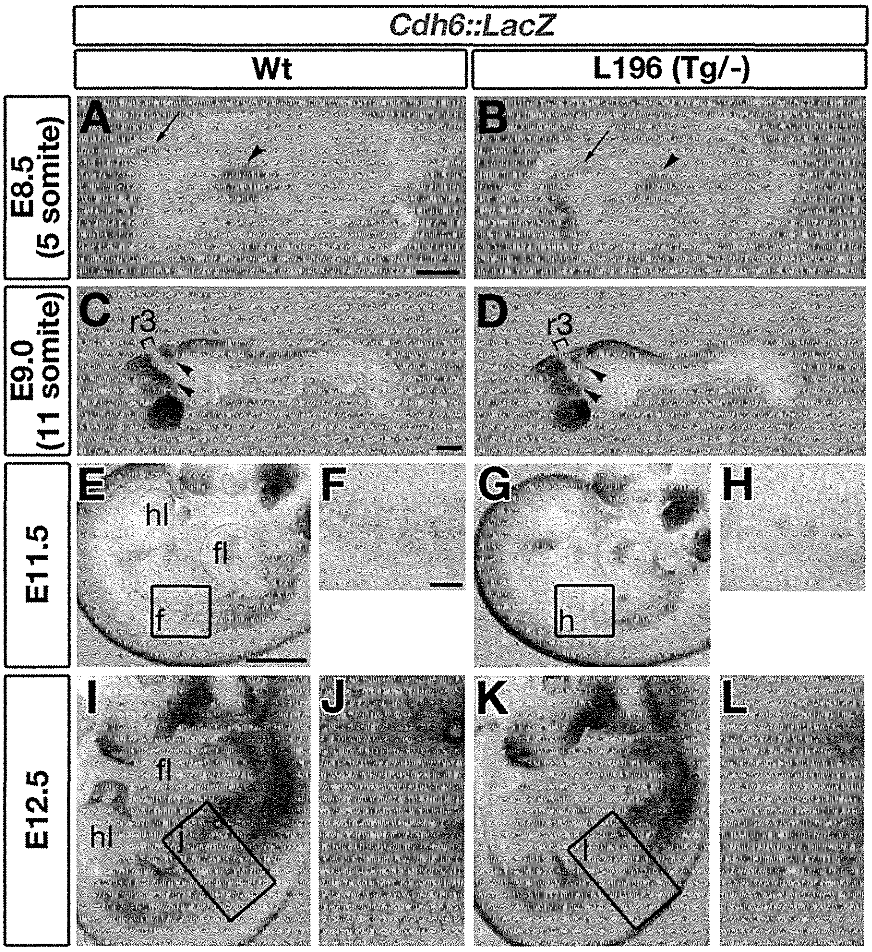

Fig. 3. Neural crest development and Schwann cell incorporation at earlier developmental stages in *SOX10-S1*-Tg L196. *SOX10-S1*-Tg Line 196 is intercrossed with a *Cdh6::LacZ*-Tg line that recapitulates *Cdh6* mRNA expression profile along the developing neural crest cells as well as differentiating Schwann cells. (A, B) Dorsal views of whole-mount stained embryos at the 5-somite stage (E8.5). Anterior is to the left. At this stage *Cdh6::LacZ* expression demarcating the cranial neural ridge (arrows) and trunk neural tube (arrowheads) is indistinguishable between L196 (Tg/−) and the Wt littermates. Scale bar, 200 μm. (C, D) Lateral views of whole-mount stained embryos at the 11-somite stage (E9.0). Anterior is to the left. *Cdh6* expression delineates emigrating cranial neural crest cells as streams at this stage. Note that the metameric migrating patterns of cranial neural crest cells (arrowheads) are still evident in embryos with both genotypes. r3, rhombomere 3; Scale bar, 200 μm. (E–H) Lateral views of the whole-mount stained embryos at E11.5. Panels F and H show higher magnifications of the area f in panel E and area h in panel G, respectively. At this stage, Schwann cell specific Cdh6::LacZ staining is almost absent in L196 (Tg/−) embryos. (I–L) Lateral views of the whole-mount stained embryos at E12.5. Panels J and L are magnified views of area j in panel I and area l in panel K, respectively. Schwann cell arrangement marked by Cdh6::LacZ staining is sparse and fuzzy in L196 (Tg/−) embryos. Scale bars, 200 μm for E, G, I, and K; 1 mm for F, H, J, and L. fl, forelimb; hl, hindlimb.

sheaths and Remak bundles could develop almost normally along the sciatic nerve, but their final morphological structure was less refined in adult *SOX10-S1*-Tg mice.

The terminal differentiation of oligodendrocyte lineage cells was delayed in postnatal SOX10-S1-Tg mouse in a manner dependent on the transgene dosage

Oligodendrocyte development was investigated in *SOX10-S1*-Tg mice. As similar to *Sox10*$^{LacZ/LacZ}$ mice (Stolt et al., 2002), oligodendrocyte lineage cells that express the transcription factor Olig2 had already become interspersed over the spinal cord of mice with each genotype by P0 (Figs. 6A–F) and reached the prospective white matter (Figs. 6G–L) in the neonatal cervical spinal cords of L55 mice. The numbers of Olig2-expressing cells were equivalent among each genotype of L55 at P0 and P3 (Fig. 6Y). On the other hand, intensity of the MBP-IR along the ventral part of the prospective white matter was significantly lower in 1–5Tg mice compared with Wt mice at P0 (Figs. 6M–R). At P3, the MBP-IR intensity tended to decrease in a manner dependent on the transgene copy number, even though only 5Tg mice have reached statistical significance in comparison with Wt and 1Tg mice (Figs. 6S–X and Z). Together, we confirmed that MBP expression along the prospective white matter was reduced in a manner dependent on copy number whereas OPCs were equally developed in 1–5Tg mice from L55.

In the brain on the B6C3 background (a hybrid of C57BL/6 and C3H/He), MBP expression was abundant in the white matter of the cerebellum and brain stem, and reached to the corpus callosum in P11 L55 2Tg and 3Tg mice, which was similar to Wt mice (Figs. 7A–C). Therefore L55-Tg mice were backcrossed with the C57BL/6 strain, because modifiers from the C57BL/6 background are known to impinge on the severity of hypoganglionosis in the *Sox10*$^{Dom/+}$ mice (Cantrell et al., 2004; Southard-Smith et al., 1999). When L55 mice were backcrossed to the third generation (C57BL/6$_{N3}$), a faint MBP-IR was observed only in the cerebellum and brain stem of 2Tg and 3Tg mice at P11, which contrasted with Wt mice (Figs. 7D–F). At P20, MBP-IR became more extensive and stronger throughout the brains including corpus callosum, hippocampus, olfactory bulbs, striatum, and cerebral cortex (Figs. 7G–I). As clearly observed in the higher magnitude images (Fig. 7J), myelination progressing into the gray matter of cerebral cortex and the pencil fibers in the striatum were present in Wt mice. In contrast, 2Tg and 3Tg mice showed only restricted and faint signals in the corpus callosum (Figs. 7K and L). In addition, the myelin fibers extending into cortex or striatum were barely observed. Electron

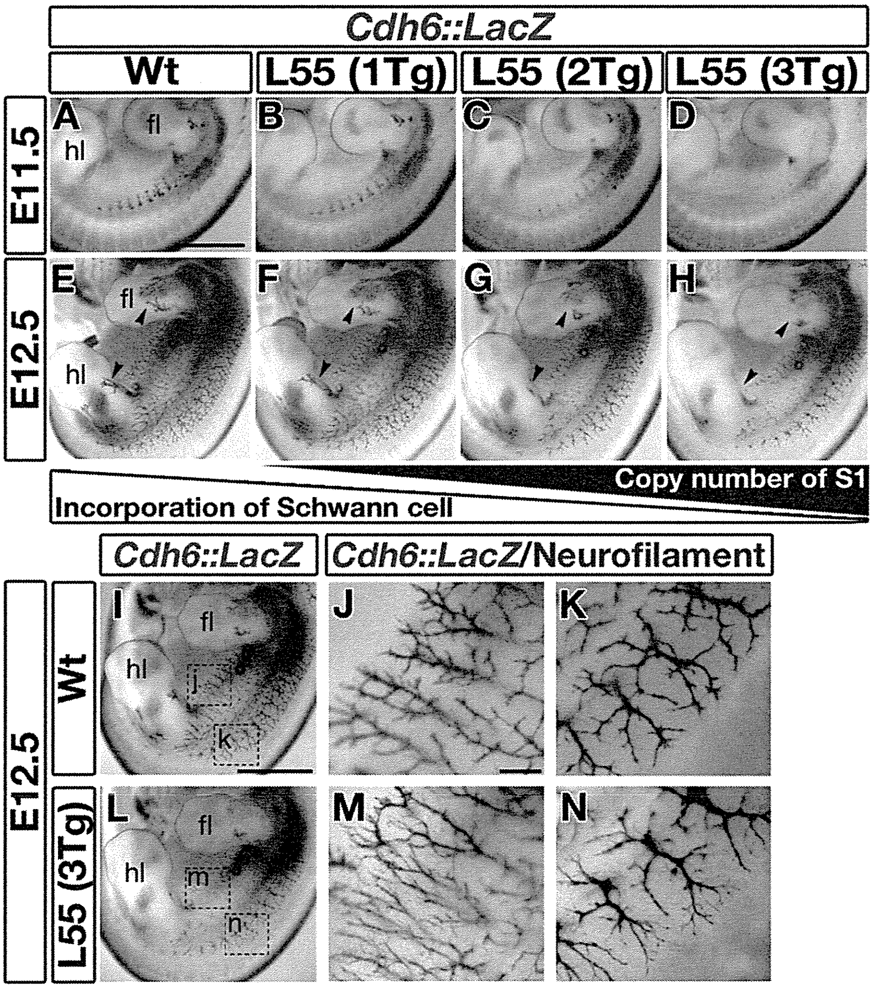

Fig. 4. Embryonic Schwann cell incorporation is retarded in a manner related to *SOX10-S1* dosage. *SOX10-S1*-Tg Line 55 (L55) was intercrossed with the *Cdh6::LacZ*-Tg line and *Cdh6::LacZ* expression was examined at E11.5 (A–D) and E12.5 (E–H). Note that Schwann-cell-specific Cdh6 expression becomes weaker and sparser with increasing *SOX10-S1* expression. Arrowheads, *Cdh6::LacZ* expressing Schwann cells incorporated into limb buds. fl, forelimb; hl, hindlimb. Scale bar, 1 mm. (I–N). *Cdh6::LacZ* stained E12.5 Wt (I) and 3Tg embryos (L) were further processed for neurofilament immunostaining that marks peripheral nerve fibers in whole-mount preparations (J, K, M, and N). Dotted areas j and k in panel I, and m and n in panel L, are enlarged in panels J and K and M and N, respectively. Noticeably, Schwann cell specific *Cdh6::LacZ* signals completely enwrap the peripheral nerves in the Wt embryo (J, K), whereas many nerve fibers or terminals remain uncovered with Cdh6::LacZ positive Schwann cells in the L55 (3Tg) embryo (M, N). Scale bars: 1 mm for I and L; 200 μm for J, K, M, and N.

microscopic analysis of the corpus callosum at P20 showed an obvious reduction in the number of myelinated axons in 3Tg mice (Figs. 7M–O). These results suggest that the *SOX10-S1* transgene certainly exerts negative effects on myelin formation in the central nervous system including the brain, which might be exacerbated by genetic factors from the C57BL/6 background.

In summary, we have concluded that the terminal differentiation of oligodendrocyte lineage cells in the developing spinal cord and brain was delayed in *SOX10-S1*-Tg mice in a manner dependent on the transgene dosage.

No apparent phenotypes emerged in the Sox10::Venus BAC Tg mice

As mentioned in the first section, overexpression of Wt SOX10 could lead to distinct pathological conditions in human (Seeherunvong et al., 2004; Polanco et al., 2010) and induced the epithelial–mesenchymal transition in the neural tube *in ovo* (Cossais et al., 2010). In contrast, the c.1400del12 mutation in the *SOX10-S1* transgene was unable to induce such transition (Cossais et al., 2010). This is probably because the mutant SOX10 protein has lost DNA binding ability and transcriptional activities to the native SOX10 binding sites (Inoue et al., 2007). Accordingly, we considered that the pathological basis of SOX10-S1 overexpression was much different from that of Wt SOX10 overexpression *in vivo*. However, it had still remained unclear if the overexpression of the *Venus* and/or other genes contained in the mouse BAC clone *RP24-85O14* (such as *Pick1*, *Baiap2l2*, and *Pla2g6*) cause the phenotypes observed in our *SOX10-S1*-Tg mouse lines. In order to finally invalidate these possibilities, we analyzed the *Sox10::Venus* BAC Tg mouse lines in which only *Venus* gene expression cassette was integrated into the Sox10 locus of the BAC clone (Fig. 8A; Shibata et al., 2010). Consequently, we ascertained no evidence of delayed incorporation of neural crest lineage cells to the peripheral nerve of E11.5 embryos ($n = 3$, Figs. 8B–D), lower MBP expression in the spinal cord at P3 ($n = 3$, Figs. 8E–G), and the hypoganglionosis at P3 ($n = 3$, Figs. 8H–J) in the *Sox10::Venus* Tg mice with 2- and 20-copy transgenes. From daily observation, neither hypopigmentation nor rotating behavior was found in both *Sox10::Venus* Tg mouse lines. We thus confirmed that the overexpression of *Venus* and/or the other genes contained in the BAC clone does not result in any of the pathological phenotypes in the *SOX10-S1*-Tg mice, providing a genuine negative control to clarify the dominant effect of SOX10-S1 protein in vivo.

Discussion

In this study, we have constructed a mouse model that recapitulates each component of the complex clinical phenotypes seen in PCWH, at least in part. In addition, we have shown the additive effect of the *SOX10 3′* extension mutation that possibly acts as a gain-of-function

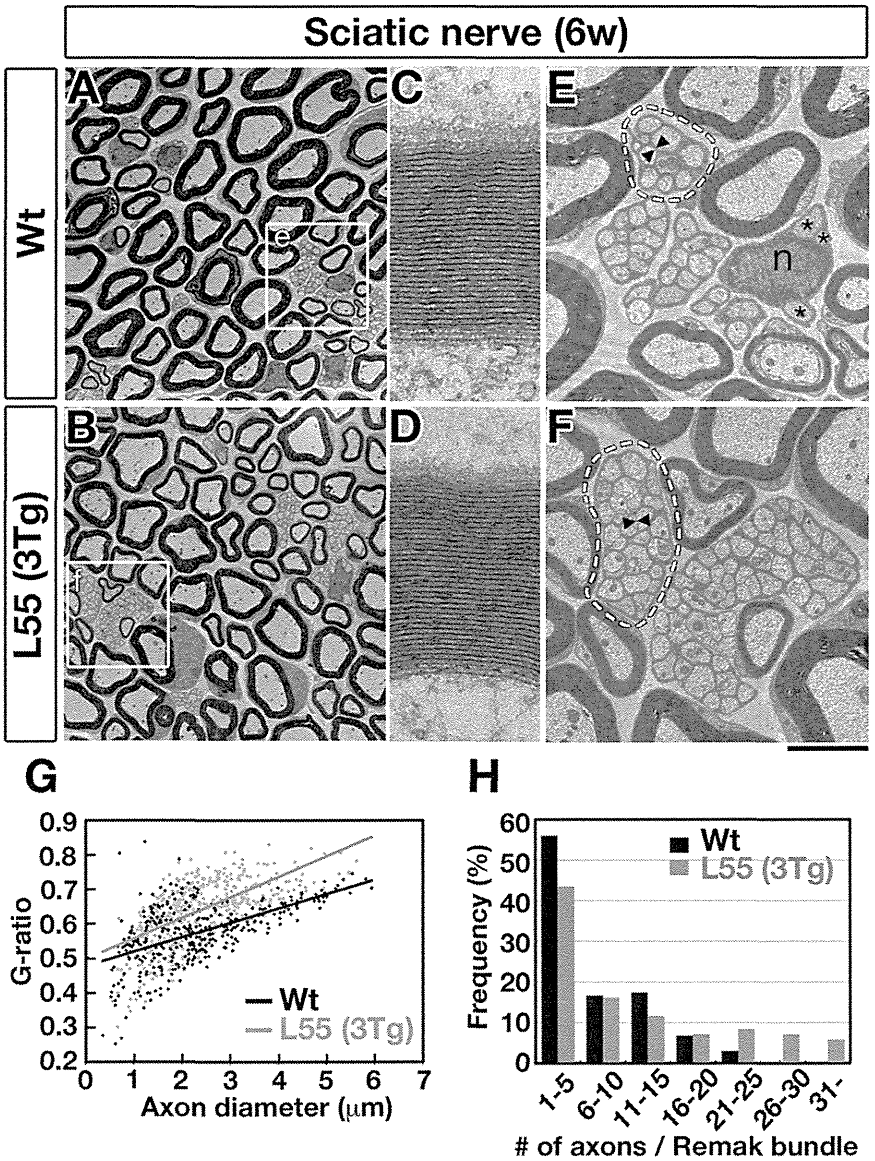

Fig. 5. Abnormal refinement in compact myelin sheaths and Remak bundles in adult *SOX10-S1*-Tg mice. (A–F) Electron microscope images of the sciatic nerves of 6-week-old (6w) mice. (B) There are few anomalous features, and the myelin sheaths are observed extensively in the panoramic view of 3Tg mice from L55 (L55-3Tg mice). (D) Higher magnification reveals the compact myelin multilayer of a myelinating Schwann cell even in L55-3Tg mice. Areas marked by white squares in A and B are magnified in E and F, respectively. (E) Several Remak bundles composed of multiple unmyelinated axons (*) are held by one nonmyelinating Schwann cell (n). In most cases, the cytoplasm of a Schwann cell separates unmyelinated axons, and the nucleus is out of the plane of section (enclosed by white broken lines in E and F). In L55 3Tg mice, some Remak bundles are enlarged and embrace more axons, and the space between axons tends to be narrower (compare the pairs of arrowheads in E and F). Scale bars: 10 μm for A and B; 200 nm for C and D; 2.8 μm for E and F. (G) Scatter plots of axon diameter and G-ratio (inner/outer diameter of the myelin sheath) measured in Wt (black dots) and L55-3Tg (gray dots). A larger G-ratio indicates thinner myelin. The black and gray lines represent the trendlines for each set of data. Linear regression between inner (axon) diameter and G-ratio shows a significant difference in slope between Wt and L55 3Tg mice (Wt: $n = 373$ myelinated axons from 3 mice, $y = 0.042x + 0.48$; L55 3Tg: $n = 420$ myelinated axons from 3 mice, $y = 0.060x + 0.50$. $F_{(1,789)} = 14.2$, $p < 0.001$ for parallel slope by ANCOVA). (H) Remak bundles are classified by based on the number of axons in a bundle, and the frequency distribution is shown (Wt: $n = 99$ bundles, L55 3Tg: $n = 64$ bundles). Remak bundles of L55-3Tg mice contain a larger number of axons in each bundle.

allele (Inoue et al, 2007). These findings provide valuable insights into the pathological basis and clinical variability of PCWH.

Genotype–phenotype studies in human patients with WS4 and PCWH have suggested that the WS4 phenotype is caused by haploinsufficiency of *SOX10*, while the more severe and complex PCWH phenotype may result from either dominant-negative or gain-of-function alleles (Inoue et al., 2004). However, the mechanisms by which the dominant action of PCWH-causing mutations affects cellular functions had not yet been determined in vivo. It was speculated that the phenotypes observed in PCWH patients are a mixture of WS4-causing haploinsufficiency and an additional dominant effect. Using BAC transgenic technique, we have eliminated the effect of haploinsufficiency from our analysis, and have successfully highlighted the dominant effect of the extension mutation alone in each PCWH-affected cell lineage (Fig. 9). These findings have provided crucial evidence that complex PCWH phenotypes likely result from additive pathogenic effect in addition to WS4-causing haploinsufficiency.

Our study has also shed light on factors associated with the clinical variability observed in PCWH patients. We showed that the additive pathogenic effect of the SOX10 mutation causes more severe cellular phenotypes. This implies that in distinct PCWH-causing mutations, different levels of pathogenic effect for each mutation may exert direct influence on the clinical severity. Despite differences between qualitative and quantitative effects, our model supports the notion that difference in the strength of dominant pathogenic effect in different mutations may influence the range of severity of PCWH phenotype. In

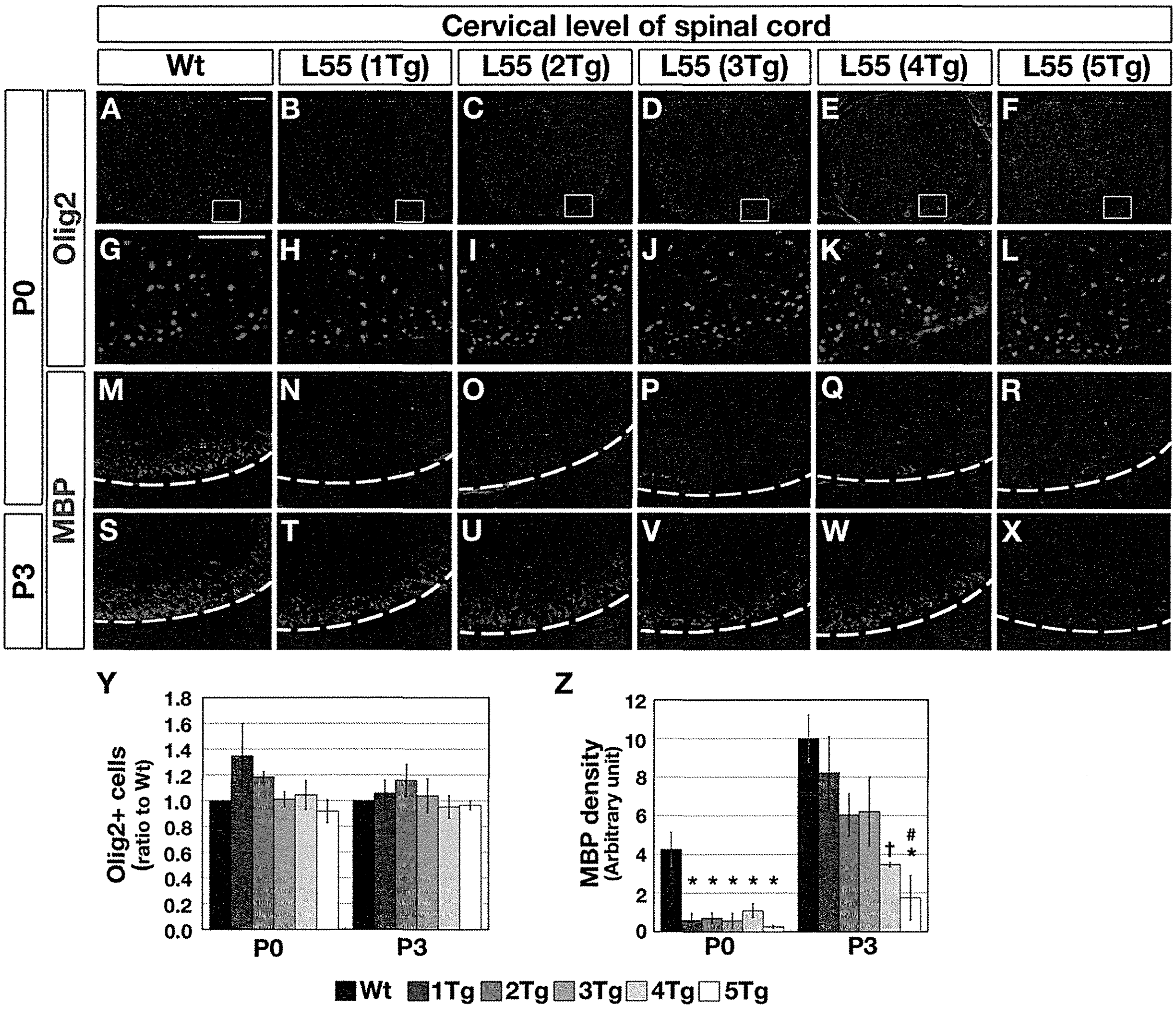

Fig. 6. Dose-dependent delay in the terminal differentiation of oligodendrocyte-lineage cells in postnatal *SOX10-S1*-Tg L55. (A–L) Olig2-positive (Olig2+) oligodendrocyte lineage cells seen in transverse sections of cervical spinal cord at postnatal day 0 (P0). (A–F) For every genotype, Olig2+ cells are well interspersed throughout the spinal cord and reach the prospective white matter (G–L, higher magnification of rectangles in A–F). (M–X) Myelin basic protein immunoreactivity (MBP-IR), a marker of commitment to becoming a myelinating oligodendrocyte, is evaluated at cervical level of the spinal cord at P0 and P3. (M) At P0, MBP-IR is observed in an adjacent section to G in Wt mice. (N–R) At P0, little MBP-IR is detected in 1–5Tg mice from L55. (S–X) At P3, MBP-IR appears even in 1–5Tg mice (T–X), but is still lower than Wt mice (S). Scale bars: 200 μm for A–F; 100 μm for G–X. (Y) Comparison of the number of Olig2+ cells in cervical spinal cord between Wt and 1–5Tg mice. There is no significant difference among genotypes ($n = 3$–5, $p > 0.05$). (Z) Comparison of the density of MBP-IR in the spinal cord between Wt and 1–5Tg mice. The MBP-IR of 1–5Tg mice is significantly lower in density than that of Wt mice at P0, and decreases at P3 in a manner dependent on *SOX10-S1* transgene dose [*: $p < 0.01$, compared with Wt mice; #: $p < 0.05$, compared with 1Tg mice; †: q-statistic between Wt and 4Tg mice (3.18) is close to significant level of 0.05 (3.22).

contrast, WS4 patients show relatively uniform clinical symptoms because different WS4-causing mutations all result in loss-of-function alleles.

The phenotypes demonstrated in Schwann cells and oligodendrocytes of the Tg mice are unique findings and provide insights into the neurological manifestations of PCWH. In the peripheral nervous system, we found that the mutant *SOX10* transgene affects the differentiation and/or incorporation of Schwann cells at the embryonic stage. Although no apparent abnormality was found in the early migration of neural crest cells at E8.5–E9.0, Schwann cell incorporation along the normally extending axons of nerve fibers was delayed at E11.5–E12.5. This probably reflects the strong influence of the synergistic expression of SOX9, which in the early developmental stage plays a dominant role in neural crest migration, but later decreases in expression while SOX10 continues to be expressed and takes over the dominant role in developmental regulation (Haldin and LaBonne, 2010). The extension of neurofilament-positive peripheral nerve axons was intact, suggesting that only Schwann cell development is affected. In the adult stage, the myelin sheath was significantly thinner in Tg mice, suggesting modest hypomyelination. Together, it is likely that the mutant *SOX10* transgene delays the myelination of Schwann cells, which is consistent with the hypomyelinating phenotype observed in some PCWH patients (Inoue et al., 2002; Parthey et al., 2012; Pingault et al., 2000). Interestingly, we observed excessive branching of unwrapped neurofilament-positive nerve (Figs. 3M and N), and also increased number of fascicles in postnatal sciatic nerves (data not shown). We speculate that this may result from delayed Schwann cell incorporation and not from a primary axonal abnormality. The increased number of nerve fascicles reported in one PCWH patient (Pingault et al., 2000) may share the same pathological basis with our Tg mice.

Some Remak bundles in the Tg mice contain larger numbers of nonmyelinated axons, which can be clustered in polyaxonal pockets. A similar but more severe finding has also been reported in a PCWH patient (Inoue et al., 2002). Although the molecular mechanism underlying this phenotype is unknown, similar features were described in mice with sensory nerve-specific ablation of *neuregulin 1* (*Nrg1*) (Fricker et al., 2009) and in mice in which the *Nrg1* signaling pathway has been disrupted in Schwann cells (Tao et al., 2009; Taveggia et al., 2005; Willem et al, 2006). Sox10 regulates transcription of *ErbB3*, a gene encoding the receptor for Nrg1, in mice (Britsch et al., 2001) and zebrafish (Prasad et al., 2011). SOX10 possibly regulates Remak bundle formation by Schwann cells, which is mediated by axon-derived Nrg1

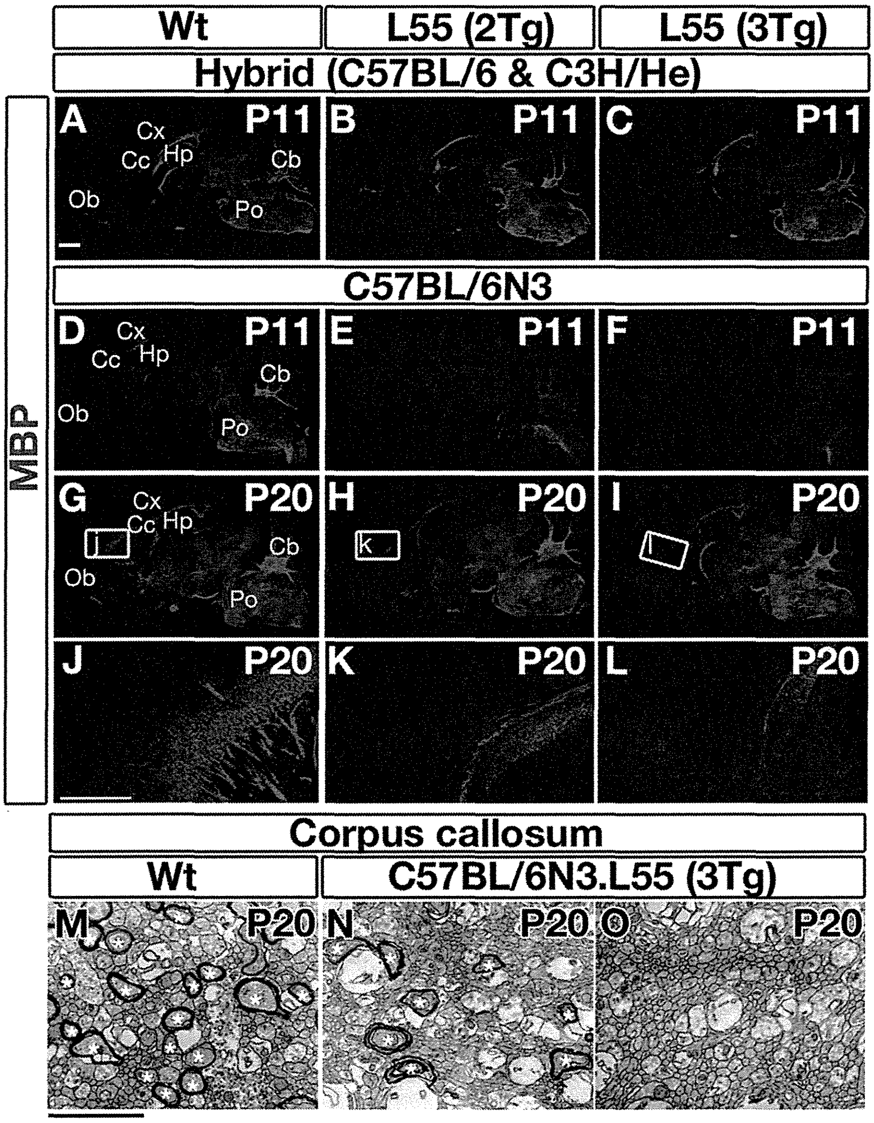

Fig. 7. Genetic background of C57BL/6 strain exacerbates the pathogenetic effect of the *SOX10-S1* transgene on brain myelination. (A–L) Myelin basic protein immunoreactivity (MBP-IR) of sagittal sections of the brain at P11 and P20 from L55 transgenic mice. (A–C) When crossed with C57BL/6 and C3H/He strains, MBP-IR of the brain is comparable among Wt, 2Tg, and 3Tg mice at P11. (D–F) L55 transgenic mice backcrossed to the C57BL/6 strain for three generations (C57BL/6_{N3}) show decreased MBP-IR in the brains of 2Tg and 3Tg mice at P11. (G–I) MBP-IR in the brains of 2Tg and 3Tg mice at P20 is more extensive than at P11, but is still less than Wt mice (J–L: magnified views of areas enclosed by white rectangles in G–I, respectively). Cc: corpus callosum, Cb: cerebellum, Cx: cerebral cortex, Hp: hippocampus, Ob: olfactory bulb, Po: pons. Scale bars: 1 mm for A–I; 500 μm for J–L (M–O). Electron microscope images of the corpus callosum at P20. Compared with Wt mice (M), myelin sheathes are decreased (N) or completely absent (O) in 3Tg mice on a C57BL/6_{N3} background. * indicates myelinating axons.

signaling, and the phenotype observed in the *SOX10-S1*-Tg mice may have resulted from dysregulation of the Nrg1–ErbB pathway.

In the central nervous system, we have shown that the mutant *SOX10* transgene delays terminal differentiation of oligodendrocytes in a dose-dependent manner in the cervical spinal cord. No reduction of Olig2-positive OPCs was evident, but MBP signal strength, presumably reflecting mature myelin formation (Stolt et al., 2002), was reduced in Tg mice at both P0 and P3. Interestingly, MBP expression was similarly diminished in the Tg mice with different copy numbers at P0, but at P3, this delay was evident only in the 5Tg animal, suggesting that the mutant transgene delays the terminal differentiation regardless of gene dosage, and the degree of delay is minimal in animals with lower copy numbers. Consistent with these findings, MBP staining of the brain of a P11 mouse with 3Tg on a B6C3 background showed no delay in myelination (Fig. 6C). However, mice with a higher proportion of C57BL/6 background showed an apparent reduction in immunoreactivity of MBP in the brain (Figs. 6D–L), suggesting that the mutant transgene also elicits a delay in the terminal differentiation of oligodendrocytes in the cortical white matter.

Although we demonstrated that the *SOX10 3′* extension mutation elicits additive dominant effects by itself in vivo, it is still unclear how this mutant protein affects the SOX10-expressing cells at the molecular level. Our previous studies in vitro have shown that the extended mutant protein has no ability to bind to DNA at the SOX binding site and to drive transcription, despite the Wt SOX10 coding sequence remaining intact (Inoue et al., 2007). The extension mutant does not interfere with the transcriptional activity of co-existent Wt SOX10 protein, suggesting that the mutant protein does not function as a dominant-negative allele. This contrasts with an apparent dominant-negative action of PCWH-causing truncating mutations, which compete with Wt protein at the target SOX10 binding sites (Inoue et al., 2004). Extensive analysis of the mutant protein has revealed that an 11-amino-acid domain (termed WR domain) in the 82-amino-acid-extended polypeptide is sufficient to express the deleterious effect of the mutant

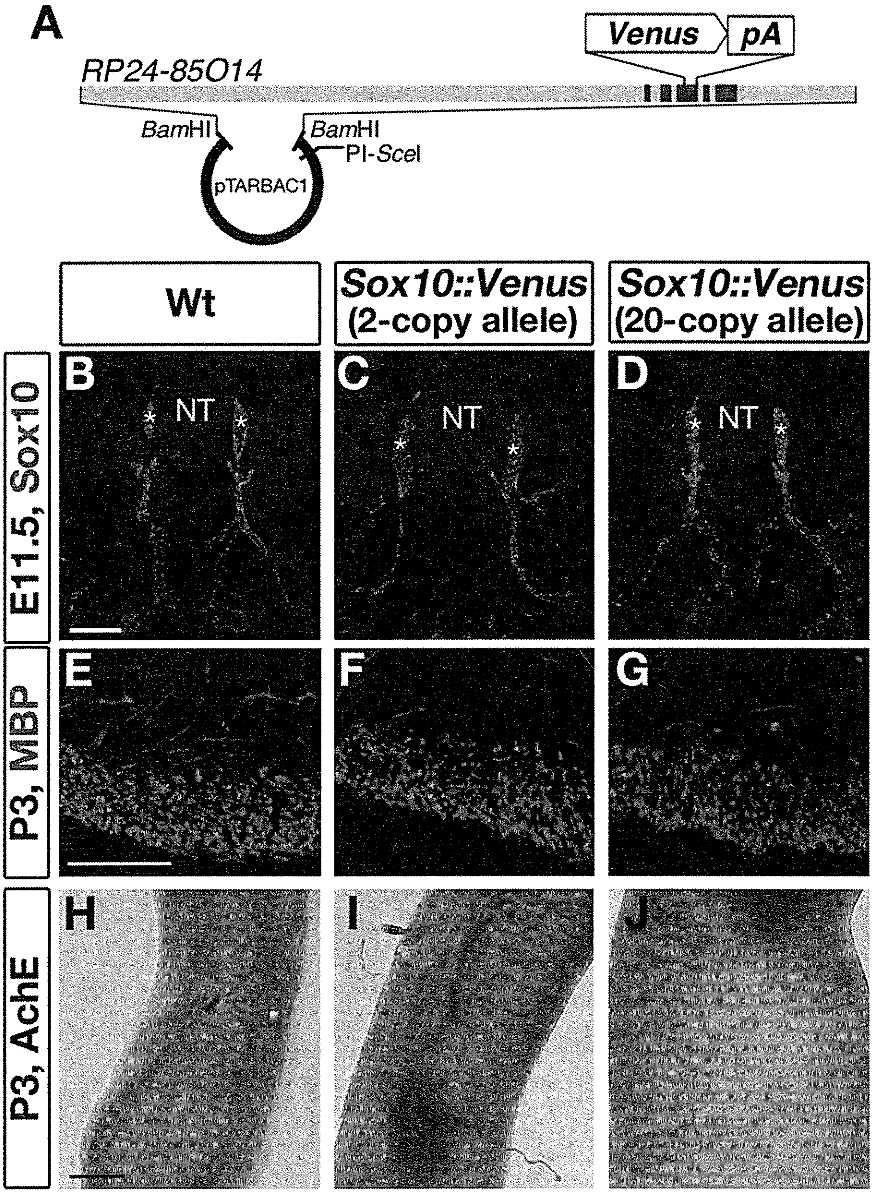

Fig. 8. No apparent phenotypes emerge in *Sox10::Venus* BAC Tg mouse lines. (A) As the genuine control, the *Sox10* locus in the *PR24-85O14* BAC clone is modified solely by the *Venus* expression cassette to generate the *Sox10::Venus* BAC Tg mouse lines (Shibata et al., 2010). (B–D) Images are transverse sections of the abdomen at E11.5. Sox10-positive cells evenly distribute along the nerve tracts in the trunk of Wt mice (B), Tg mice with a 2-copy-transgene allele (C) and a 20-copy-transgene allele (D). NT: neural tube. Asterisks: dorsal loot ganglia. (E–G) MBP-IR of ventral part of the cervical spinal cord at P3 is arranged. MBP highly expressed regardless of the genotypes at this stage. (H–J) Distal parts of the large intestines are stained by acetylcholine esterase (AchE) histochemistry. No hypoganglionosis is observed in *Sox10::Venus* Tg mouse lines. Scale bars: 100 μm for B–D and for E–G; 200 μm for H–J.

protein, suggesting that gain-of-function is the most likely mechanism underlying the *SOX10 3′* extension mutation (Inoue et al., 2007). Our findings in the Tg mice confirmed that the extension mutant is also deleterious in vivo, and this harmful effect is dependent on copy number.

Conclusions

We have reported the first mouse model to carry a PCWH-causing *SOX10* mutation that presumably acts as a gain-of-function allele. Recombinant BAC transgenic technology enabled the effects of gain-of-function and haploinsufficiency to be uncoupled (Fig. 9). We observed developmental abnormalities in each of four cell lineages associated with the PCWH phenotype. All these abnormalities are solely caused by the mutant transgene and show a dosage effect. We have thus provided an analytical basis for elucidating the pathogenesis of PCWH, and crucial evidence suggesting that the additive dominant effect of the PCWH-causing *SOX10* mutation, in combination with haploinsufficiency, is the likely mechanism underlying the complex neurological phenotypes of human PCWH patients.

Funding

This study was funded in part by grants from the Health and Labour Sciences Research Grants, Research on Intractable Diseases (H24-Nanchitou-Ippan-072 and H26-Itaku(Nan)-Ippan-023, to K.I.), Grants-in-Aid for Scientific Research from the Ministry of Education, Culture, Sports, Science, and Technology, Japan (KAKENHI: 24510280 to Y. U. I.; 21500333 and 24300130 to T.I.; 21390103, 23659531, and 25670485 to K.I.), Intramural Research Grants for Neurological and Psychiatric Disorders of NCNP (24-12, 26-9, and 27-7 to T.I.; 24-9, 25-4, and 27-7 to K.I.) and Takeda Science Foundation (to T.I. and K.I.)

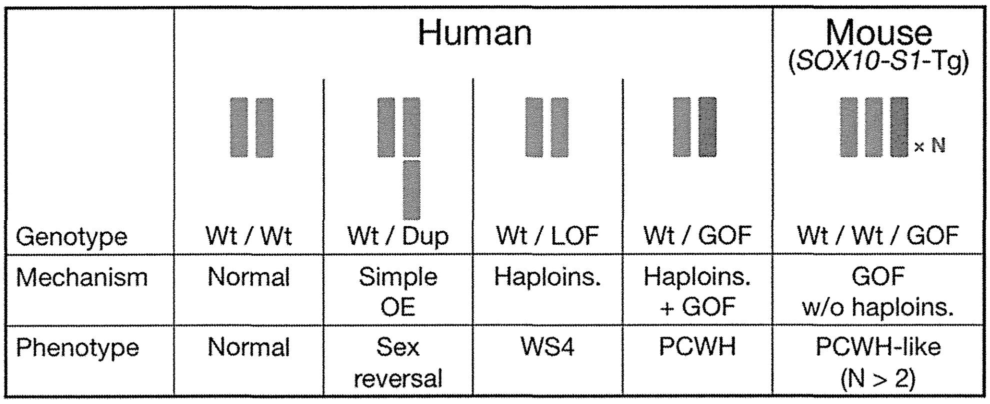

	Human				Mouse (*SOX10-S1*-Tg)
					× N
Genotype	Wt / Wt	Wt / Dup	Wt / LOF	Wt / GOF	Wt / Wt / GOF
Mechanism	Normal	Simple OE	Haploins.	Haploins. + GOF	GOF w/o haploins.
Phenotype	Normal	Sex reversal	WS4	PCWH	PCWH-like (N > 2)

Fig. 9. A schema for SOX10 alleles in human patients and Tg mouse models. In human, there are normally 2-copies of Wt *SOX10* alleles shown by the light blue bars. The *SOX10* mutations cause autosomal-dominant diseases: duplication (Dup) of *SOX10* leads to the sex reversal (Seeherunvong et al., 2004), while loss-of-function (LOF) allele shown by the gray bar leads to haploinsufficiency (haploins.), causing WS4. The PCWH-causing allele harboring c.1400del12 mutation, shown by the red bar, is our focus in this study. The C-terminus-extended SOX10 protein resulting from this mutation has neither DNA binding ability nor transcriptional activities to the native SOX10 binding sites (Inoue et al., 2007). In addition, it exerts no dominant-negative effect in vitro, and an 11 amino acid domain in the extension conveys deleterious property, collectively suggesting that gain-of-function (GOF) is the likely mechanism for this PCWH-causing mutation (Inoue et al., 2007). Other PCWH-causing truncating mutations are not depicted in this schema. In the present study, we have generated the *SOX10-S1*-Tg mouse line, in which endogenous two *Sox10* alleles remain intact and the human GOF alleles are additionally introduced by transgenesis, to highlight that the additive effects of GOF alleles can solely and dominantly impinge on pigmentation, auditory sensing, enteric nerve plexus formation, and myelination of the peripheral and central nervous systems in a manner dependent on the transgene dosage.

Conflict of interest statement

No conflict of interest is apparent.

Author contributions

K.I., T.I., and C.A. designed the project with help from S.K. and Y-i. G. Y.I., N.I., Y.U.I., S.N., Y.M., M.I., T.O., J.A., Y.W.T. and T.I. performed the experiments and Y.I., N.I., Y.U.I., C.A., T.I., and K.I. analyzed the data. Y.I., T.I., and K.I. wrote the manuscript.

Acknowledgments

We thank Dr. Li-Hua Yu, Ms. Hitomi Osakabe, Ms. Eriko Hirano and Ms. Yoriko Kojima (NCNP) for their technical help.

Appendix A. Supplementary data

Supplementary data to this article can be found online at http://dx.doi.org/10.1016/j.nbd.2015.04.013.

References

Anzini, P., et al., 1997. Structural abnormalities and deficient maintenance of peripheral nerve myelin in mice lacking the gap junction protein connexin 32. J. Neurosci. 17, 4545–4551.

Bondurand, N., Sham, M.H., 2013. The role of SOX10 during enteric nervous system development. Dev. Biol. 382, 330–343.

Bondurand, N., et al., 2007. Deletions at the SOX10 gene locus cause Waardenburg syndrome types 2 and 4. Am. J. Hum. Genet. 81, 1169–1185.

Bremer, M., et al., 2011. Sox10 is required for Schwann-cell homeostasis and myelin maintenance in the adult peripheral nerve. Glia 59, 1022–1032.

Britsch, S., et al., 2001. The transcription factor Sox10 is a key regulator of peripheral glial development. Genes Dev. 15, 66–78.

Cantrell, V.A., et al., 2004. Interactions between Sox10 and EdnrB modulate penetrance and severity of aganglionosis in the Sox10Dom mouse model of Hirschsprung disease. Hum. Mol. Genet. 13, 2289–2301.

Chew, L.J., Gallo, V., 2009. The Yin and Yang of Sox proteins: activation and repression in development and disease. J. Neurosci. Res. 87, 3277–3287.

Copeland, N.G., et al., 2001. Recombineering: a powerful new tool for mouse functional genomics. Nat. Rev. Genet. 2, 769–779.

Cossais, F., et al., 2010. SOX10 structure-function analysis in the chicken neural tube reveals important insights into its role in human neurocristopathies. Hum. Mol. Genet. 19, 2409–2420.

Fricker, F.R., et al., 2009. Sensory axon-derived neuregulin-1 is required for axoglial signaling and normal sensory function but not for long-term axon maintenance. J. Neurosci. 29, 7667–7678.

Gubbay, J., et al., 1990. A gene mapping to the sex-determining region of the mouse Y chromosome is a member of a novel family of embryonically expressed genes. Nature 346, 245–250.

Haldin, C.E., LaBonne, C., 2010. SoxE factors as multifunctional neural crest regulatory factors. Int. J. Biochem. Cell Biol. 42, 441–444.

Herbarth, B., et al., 1998. Mutation of the Sry-related Sox10 gene in Dominant megacolon, a mouse model for human Hirschsprung disease. Proc. Natl. Acad. Sci. U. S. A. 95, 5161–5165.

Inagaki, M., et al., 2006. Characteristic findings of auditory brainstem response and otoacoustic emission in the Bronx waltzer mouse. Brain Dev. 28, 617–624.

Inoue, T., et al., 1997. Cadherin-6 expression transiently delineates specific rhombomeres, other neural tube subdivisions, and neural crest subpopulations in mouse embryos. Dev. Biol. 183, 183–194.

Inoue, K., et al., 1999. Myelin deficiencies in both the central and the peripheral nervous systems associated with a SOX10 mutation. Ann. Neurol. 46, 313–318.

Inoue, K., et al., 2002. Congenital hypomyelinating neuropathy, central dysmyelination, and Waardenburg–Hirschsprung disease: phenotypes linked by SOX10 mutation. Ann. Neurol. 52, 836–842.

Inoue, K., et al., 2004. Molecular mechanism for distinct neurological phenotypes conveyed by allelic truncating mutations. Nat. Genet. 36, 361–369.

Inoue, K., et al., 2007. Translation of SOX10 3′ untranslated region causes a complex severe neurocristopathy by generation of a deleterious functional domain. Hum. Mol. Genet. 16, 3037–3046.

Inoue, T., et al., 2008. Analysis of mouse Cdh6 gene regulation by transgenesis of modified bacterial artificial chromosomes. Dev. Biol. 315, 506–520.

Kamachi, Y., Kondoh, H., 2013. Sox proteins: regulators of cell fate specification and differentiation. Development 140, 4129–4144.

Kuhlbrodt, K., et al., 1998. Sox10, a novel transcriptional modulator in glial cells. J. Neurosci. 18, 237–250.

Lee, E.C., et al., 2001. A highly efficient Escherichia coli-based chromosome engineering system adapted for recombinogenic targeting and subcloning of BAC DNA. Genomics 73, 56–65.

Mollaaghababa, R., Pavan, W.J., 2003. The importance of having your SOX on: role of SOX10 in the development of neural crest-derived melanocytes and glia. Oncogene 22, 3024–3034.

Niemann, S., et al., 2000. Uncoupling of myelin assembly and Schwann cell differentiation by transgenic overexpression of peripheral myelin protein 22. J. Neurosci. 20, 4120–4128.

Parthey, K., et al., 2012. SOX10 mutation with peripheral amyelination and developmental disturbance of axons. Muscle Nerve 45, 284–290.

Perea, J., et al., 2001. Induced myelination and demyelination in a conditional mouse model of Charcot–Marie–Tooth disease type 1A. Hum. Mol. Genet. 10, 1007–1018.

Pingault, V., et al., 1998. SOX10 mutations in patients with Waardenburg–Hirschsprung disease. Nat. Genet. 18, 171–173.

Pingault, V., et al., 2000. Peripheral neuropathy with hypomyelination, chronic intestinal pseudo-obstruction and deafness: a developmental "neural crest syndrome" related to a SOX10 mutation. Ann. Neurol. 48, 671–676.

Pingault, V., et al., 2002. SOX10 mutations in chronic intestinal pseudo-obstruction suggest a complex physiopathological mechanism. Hum. Genet. 111, 198–206.

Pingault, V., et al., 2013. Loss-of-function mutations in SOX10 cause Kallmann syndrome with deafness. Am. J. Hum. Genet. 92, 707–724.

Polanco, J.C., et al., 2010. Sox10 gain-of-function causes XX sex reversal in mice: implications for human 22q-linked disorders of sex development. Hum. Mol. Genet. 19, 506–516.

Prasad, M.K., et al., 2011. SOX10 directly modulates ERBB3 transcription via an intronic neural crest enhancer. BMC Dev. Biol. 11, 40.

Rehberg, S., et al., 2002. Sox10 is an active nucleocytoplasmic shuttle protein, and shuttling is crucial for Sox10-mediated transactivation. Mol. Cell. Biol. 22, 5826–5834.

Runker, A.E., et al., 2004. Pathology of a mouse mutation in peripheral myelin protein P0 is characteristic of a severe and early onset form of human Charcot–Marie–Tooth type 1B disorder. J. Cell Biol. 165, 565–573.

Seeherunvong, T., et al., 2004. 46,XX sex reversal with partial duplication of chromosome arm 22q. Am. J. Med. Genet. A 127A, 149–151.

Sereda, M., et al., 1996. A transgenic rat model of Charcot–Marie–Tooth disease. Neuron 16, 1049–1060.

Sham, M.H., et al., 2001. Novel mutations of SOX10 suggest a dominant negative role in Waardenburg–Shah syndrome. J. Med. Genet. 38, E30.

Shibata, S., et al., 2010. Sox10-Venus mice: a new tool for real-time labeling of neural crest lineage cells and oligodendrocytes. Mol. Brain 3, 31.

Southard-Smith, E.M., et al., 1998. Sox10 mutation disrupts neural crest development in Dom Hirschsprung mouse model. Nat. Genet. 18, 60–64.

Southard-Smith, E.M., et al., 1999. The Sox10(Dom) mouse: modeling the genetic variation of Waardenburg–Shah (WS4) syndrome. Genome Res. 9, 215–225.

Stolt, C.C., et al., 2002. Terminal differentiation of myelin-forming oligodendrocytes depends on the transcription factor Sox10. Genes Dev. 16, 165–170.

Tao, Y., et al., 2009. Erbin regulates NRG1 signaling and myelination. Proc. Natl. Acad. Sci. U. S. A. 106, 9477–9482.

Taveggia, C., et al., 2005. Neuregulin-1 type III determines the ensheathment fate of axons. Neuron 47, 681–694.

Touraine, R.L., et al., 2000. Neurological phenotype in Waardenburg syndrome type 4 correlates with novel SOX10 truncating mutations and expression in developing brain. Am. J. Hum. Genet. 66, 1496–1503.

Willem, M., et al., 2006. Control of peripheral nerve myelination by the beta-secretase BACE1. Science 314, 664–666.

Wrabetz, L., et al., 2006. Different intracellular pathomechanisms produce diverse Myelin Protein Zero neuropathies in transgenic mice. J. Neurosci. 26, 2358–2368.

ELSEVIER

Brain & Development 38 (2016) 571–580

BRAIN & DEVELOPMENT
Official Journal of the Japanese Society of Child Neurology

www.elsevier.com/locate/braindev

Original article

The magnetic resonance imaging spectrum of Pelizaeus–Merzbacher disease: A multicenter study of 19 patients

Kaoru Sumida [a,b], Ken Inoue [c], Jun-ichi Takanashi [d], Masayuki Sasaki [e], Kenji Watanabe [f], Motomasa Suzuki [g], Hirokazu Kurahashi [g,h], Taku Omata [i], Manabu Tanaka [j], Kenji Yokochi [k], Jun Iio [l], Kuniaki Iyoda [m], Toru Kurokawa [n], Muneaki Matsuo [o], Tamotu Sato [p], Akiko Iwaki [q], Hitoshi Osaka [r,s], Kenji Kurosawa [t], Toshiyuki Yamamoto [u], Naomichi Matsumoto [v], Norihide Maikusa [w], Hiroshi Matsuda [w], Noriko Sato [a,*]

[a] *Department of Radiology, National Center Hospital of Neurology and Psychiatry, Kodaira, Tokyo, Japan*
[b] *Department of Radiology, Graduate School of Medicine and Faculty of Medicine, The University of Tokyo, Bunkyo-ku, Tokyo, Japan*
[c] *Department of Mental Retardation and Birth Defect Research, National Institute of Neuroscience, National Center of Neurology and Psychiatry, Kodaira, Tokyo, Japan*
[d] *Department of Pediatrics, Tokyo Women's Medical University Yachiyo Medical Center, Yachiyo, Chiba, Japan*
[e] *Department of Pediatrics, National Center Hospital of Neurology and Psychiatry, Kodaira, Tokyo, Japan*
[f] *Division of Pediatrics, Minami Kyushu National Hospital, Aira, Kagoshima, Japan*
[g] *Department of Pediatric Neurology, Aichi Prefectural Colony Central Hospital, Kasugai, Aichi, Japan*
[h] *Department of Pediatric Neurology, Aichi Medical University Hospital, Nagakute, Aichi, Japan*
[i] *Division of Child Neurology, Chiba Children's Hospital, Midori-ku, Chiba, Japan*
[j] *Department of Neurology, Saitama Children's Medical Center, Iwatsuki-ku, Saitama, Japan*
[k] *Department of Pediatrics, Seirei Mikatahara General Hospital, Hamamatsu, Shizuoka, Japan*
[l] *Department of Pediatrics, Hyogo Prefectural Amagasaki General Medical Center, Amagasaki, Hyogo, Japan*
[m] *Department of Pediatrics, Hiroshima City Hospital, Naka-ku, Hiroshima, Japan*
[n] *Department of Pediatrics, Seiai Rehabilitation Hospital, Onojo, Fukuoka, Japan*
[o] *Department of Pediatrics, Faculty of Medicine, Saga University, Saga, Japan*
[p] *Department of Pediatrics, Kanazawa Disabled Children's Hospital, Kanazawa, Ishikawa, Japan*
[q] *Medical Institute of Bioregulation, Kyusyu University, Higashi-ku, Fukuoka, Japan*
[r] *Department of Pediatrics, Jichi Medical University, Shimotsuke, Tochigi, Japan*
[s] *Division of Neurology, Kanagawa Children's Medical Center, Minami-ku, Yokohama, Japan*
[t] *Division of Genetics, Kanagawa Children's Medical Center, Minami-ku, Yokohama, Japan*
[u] *Institute for Integrated Medical Science, Tokyo Women's Medical University, Shinjuku-ku, Tokyo, Japan*
[v] *Department of Human Genetics, Yokohama City University Graduate School of Medicine, Kanazawa-ku, Yokohama, Japan*
[w] *Integrative Brain Imaging Center, National Center of Neurology and Psychiatry, Kodaira, Tokyo, Japan*

Received 26 August 2015; received in revised form 9 December 2015; accepted 10 December 2015

Abstract

Purpose: We retrospectively evaluated the imaging spectrum of Pelizaeus–Merzbacher disease (PMD) in correlation with the clinical course and genetic abnormality.

---

* Corresponding author at: Department of Radiology, National Center Hospital of Neurology and Psychiatry, 4-1-1 Ogawahigashi-cho, Kodaira, Tokyo 187-8551, Japan. Tel.: +81 042 341 2711; fax: +81 042 346 2094.
E-mail address: snoriko@ncnp.go.jp (N. Sato).

http://dx.doi.org/10.1016/j.braindev.2015.12.007

Methods: We collected the magnetic resonance imaging (MRI) findings of 19 genetically proven PMD patients (all males, aged 0–29 years old) using our integrated web-based MRI data collection system from 14 hospitals. The patterns of hypomyelination were determined mainly by the signals of the cerebrum, corticospinal tract, and brainstem on T2-weighted images (T2WI). We assessed the degree of myelination age on T1-weighted images (T1WI) and T2WI independently, and we evaluated cerebellar and callosal atrophy. The clinical severity and genetic abnormalities (causal mutations of the proteolipid protein gene *PLP1*) were analyzed together with the imaging findings.

Results: The clinical stage tended to be more severe when the whole brainstem, or corticospinal tract in the internal capsule showed abnormally high intensity on T2WI. Diffuse T2-high signal of brainstem was observed only in the patients with *PLP1* point mutation. Myelination age "before birth" on T1WI is a second manifestation correlated with the clinically severe phenotypes. On the other hand, eight patients whose myelination ages were >4 months on T1WI were associated with mild clinical phenotypes. Four of them showed almost complete myelination on T1WI with a discrepancy in myelination age between T1WI and T2WI. A random and patchy pattern of myelination on T2WI was noted in one patient with *PLP1* point mutation. Advanced myelination was observed in three of the seven followed-up patients. Four patients had atrophy of the cerebellum, and 17 patients had atrophy of the corpus callosum.

Conclusion: Our multicenter study has demonstrated a wide variety of imaging findings of PMD. Signal intensity of brainstem and corticospinal tract of internal capsule would be the points to presume clinical severity in PMD patients. The spectrum of MRI findings should be kept in mind to diagnose PMD and to differentiate from other demyelinating leukodystrophies.

Keywords: Pelizaeus–Merzbacher disease; Hypomyelination; Magnetic resonance imaging; Proteolipid protein, *PLP1* duplication; *PLP1* point mutation

---

1. Introduction

Pelizaeus–Merzbacher disease (PMD) is the most common form of hypomyelinating leukodystrophy, and it is characterized by deficit myelin formation in the central nervous system (CNS) [1,2]. PMD is primarily caused by mutations in the *PLP1* gene, which encodes proteolipid protein 1, a major myelin membrane protein. *PLP1* is located in Xq22.2, and thus PMD patients show X-linked recessive inheritance, with only males being affected [3–7].

Brain magnetic resonance imaging (MRI) is a strong tool to visualize the process of normal and abnormal myelination. T2-weighted images (T2WI) in particular has demonstrated highly sensitive detection of these processes. Myelination in the CNS starts 2 months before birth and requires at least 2 years to be completed, but it continues to develop until adolescence [8–11]. During the beginning of normal myelination, T1-weighted images (T1WI) proceed to turn from low to high intensity in the myelinating white matter compared to the cortex. Subsequently, the intensity of T2WI changes from high to iso-intensity, then turns to low intensity at the completion of the myelination. Accordingly, in the brain MRI of patients with hypomyelinating leukodystrophy in which the pathological arrest of myelination occurs, the level of hypomyelination can be determined by evaluating this myelination process [11]. Diffuse high intensity on T2WI in the cerebral white matter is a key finding for the diagnosis of PMD.

Because PMD is a rare disease (i.e., 1.45 per 100,000 male live births [12]), it is difficult to perform an imaging study involving a large number of PMD patients in one institute. To address this problem, we set up an MRI data collecting system in 2013 using a web-based platform, termed IBISS (Integrative Brain Imaging Support System), which enables the submission and browsing of imaging and clinical data through the Internet to promote collaborative clinical studies of rare neurological disorders. Using the IBISS system, we have collected brain MRI of findings patients with congenital hypomyelinating leukodystrophies, including those of 19 PMD patients treated at 14 hospitals (all in Japan). With these patients' data, we assessed the degree of hypomyelination not only on T2WI but also on T1WI, which had not been emphasized previously. In this multicenter study, we accessed the degree of myelination on both T1WI and T2WI, the type of mutations, the clinical severity, and the serial MRI changes of PMD patients.

2. Materials and methods

2.1. Data collection

This retrospective study was approved by Institutional Review Board at the National Center of Neurology and Psychiatry, Tokyo. Brain MRIs of congenital hypomyelinating leukodystrophy patients were collected in the Digital Imaging and Communication in Medicine (DICOM) format submitted through the Internet or as recorded compact disks. Personal information of the patients was eliminated from the data before the submission. Clinical information was also submitted as a data sheet.

2.2. Patients

We have collected clinical and MRI data of 40 patients with congenital hypomyelinating leukodystrophies from 18 hospitals collaborating with the IBISS from 2011 to 2014. Among the 40 patients, 27 were clinically diagnosed as having PMD, representing the most common diagnosis in our cohort. Of these 27 patients, we excluded the two patients who declined *PLP1* genetic testing and the six patients who had no *PLP1* mutation. As a consequence, 19 patients with genetically proven PMD who had been admitted to 14 Japanese hospitals were enrolled. All MRI scans had been obtained for regular patient care. Axial T1WI and T2WI findings were available for all patients. The number of MR examinations ranged from 1 to 3 times. Multiple examinations were performed in seven cases.

We integrated the patients' clinical information including age at enrollment, age at onset, age at MR assessment(s), family history, genetic testing results, and electrophysiological examination in a datasheet. Clinical severity was evaluated at the time of enrollment, according to the classification proposed by Cailloux et al. [5]

2.3. *PLP1 mutation analysis*

Mutation screening was performed as a part of the diagnostic evaluation at different diagnostic laboratories with informed consent obtained from each patient or the patient's family. Each patient's genetic analysis results were obtained as a part of the clinical information. In general, quantitative polymerase chain reaction (PCR), multiplex ligation-dependent probe amplification (MLPA) or fluorescence in situ hybridization (FISH) had been used for the evaluation of *PLP1* genomic duplication and deletion. Each exonic region with adjacent splicing junctions was amplified by PCR and directly sequenced.

Table 1
Timetable of normal myelination used for MRI assessment.

Age (mos.)	Hyperintensity on T1WI	Hypointensity on T2WI
Birth	Posterior limb of internal capsule Optic radiation	
2	Anterior limb of internal capsule	Posterior limb of internal capsule
4	Splenium of corpus callosum	Optic radiation
6	Genu of corpus callosum Fornix	Splenium of corpus callosum
8	Occipital subcortical U-fiber	Anterior limb of internal capsule Fornix Genu of corpus callosum
12	Frontal subcortical U-fiber Temporal subcortical U-fiber	Early occipital subcortical U-fiber
18		Entire occipital subcortical U-fiber
24		Frontal subcortical U-fiber Temporal subcortical U-fiber

2.4. Radiological evaluation

We performed a radiological evaluation using the first MRI examination in each patient. Two experienced neuroradiologists independently evaluated the type and age of myelination in PMD patients. Nezu et al. determined the types of hypomyelination according to high signal areas on T2WI: Type I, diffuse cerebral and corticospinal high signals; Type II, diffuse cerebral high signals without corticospinal lesions; and Type III, patchy cerebral high signals [13]. Although they did not clearly define the site where corticospinal high signals were evaluated, they might regard a couple of T2 high signals in the pons as a marker of corticospinal lesions judging by their figures. In this study, we evaluated the intensity of the posterior one third of the posterior limb in the internal capsule, referring to corticospinal myelination, because it is difficult to clearly discriminate corticospinal tract from other structures in the brainstem. Therefore, we used modified types to evaluate the hypomyelination as follows: Type A, diffuse cerebral T2 high signals and corticospinal T2 high signals in the internal capsules; Type B, diffuse cerebral T2 high signals with corticospinal T2 low signals in the internal capsules; and Type C, patchy cerebral T2 high signals. Abnormal T2 high signals in the brainstem were also assessed as diffuse, partial, or none.

The degree of myelination age was defined by the established timetable of normal myelination (Table 1) on both T1WI and T2WI, independently [14]. Gaps in myelination age that were >4 months between T2WI and T1WI were considered positive. Discordant findings were discussed in detail and reevaluated to meet an accordant interpretation. The neuroradiological assessment also included atrophy of the cerebellum and the corpus callosum. When multiple MRI studies were available for a patient, the first MRI was evaluated as the imaging findings and the sequential imaging evaluation was added. The relationship between the type and degree of myelination and clinical severity was evaluated.

3. Results

The clinical and MR findings of the 19 patients are shown in Table 2. The age at enrollment ranged from 0 to 29 years old (median 9 years). Ten patients had a duplication of the *PLP1* gene, and nine had a point